A block-based numerical strategy for modeling the dynamic out-of-plane behavior of unreinforced brick masonry walls

Ghezelbash, Amirhossein; D'Altri, Antonio Maria; Sharma, Satyadhrik; Lourenço, Paulo B.; Rots, Jan G.; Messali, Francesco

DOI
10.1007/s11012-024-01899-8

Publication date
2024

Document Version
Final published version

Published in
Meccanica

Citation (APA)
Ghezelbash, A., D'Altri, A. M., Sharma, S., Lourenço, P. B., Rots, J. G., & Messali, F. (2024). A block-based numerical strategy for modeling the dynamic out-of-plane behavior of unreinforced brick masonry walls. *Meccanica*, *60*(7), 2069-2105. https://doi.org/10.1007/s11012-024-01899-8

Meccanica
https://doi.org/10.1007/s11012-024-01899-8

RESEARCH

A block-based numerical strategy for modeling the dynamic out-of-plane behavior of unreinforced brick masonry walls

Amirhossein Ghezelbash · Antonio Maria D'Altri · Satyadhrik Sharma · Paulo B. Lourenço · Jan G. Rots · Francesco Messali

Received: 16 July 2024 / Accepted: 14 October 2024

Abstract In this paper, a numerical procedure is proposed to simulate the dynamic out-of-plane response of unreinforced masonry (URM) walls. A state-of-the-art damaging block-based model, originally developed for quasi-static simulations, is extended for the first time in a dynamic regime. The blocks are represented using solid 3D finite elements governed by a plastic-damage constitutive law for both tension and compression. A cohesive-frictional contact-based formulation is used to account for interactions between the blocks. A simplified mechanical characterization is formulated to improve efficiency in wall-level analyses. Dynamic simulation is performed using a generalized HHT-α direct integration implicit solver and by implementing Rayleigh damping in the bulk. Such consideration allows the use of both mass and stiffness proportional terms of the Rayleigh damping without compromising efficiency. The strategy is applied to simulate incremental dynamic experiments performed on full-scale walls, showing good agreement between numerical and experimental results. The calibrated numerical model is then optimized to reduce computational effort while maintaining accuracy. The optimized model is used to investigate the effect of relative support motion on the one-way bending out-of-plane seismic response of URM walls, demonstrating the potential of the modeling strategy to explore the effect of boundary conditions that occur in real buildings but are often overlooked in laboratory experiments. This investigation also explores the adequacy of simplifications in capturing the effect of relative support motion, which can be adopted for simple modeling strategies commonly used in standard engineering practice.

Keywords Masonry · Dynamic · Out-of-plane · One-way bending · Rayleigh damping · Differential motions

A. Ghezelbash (✉) · S. Sharma · J. G. Rots · F. Messali
Faculty of Civil Engineering and Geosciences, Delft University of Technology, Delft, The Netherlands
e-mail: a.ghezelbash@tudelft.nl

A. M. D'Altri
Department of Civil, Chemical, Environmental and Materials Engineering, University of Bologna, Bologna, Italy

P. B. Lourenço
Department of Civil Engineering, University of Minho, Guimarães, Portugal

1 Introduction

Unreinforced masonry (URM) is one of the world's oldest building materials, and yet it still finds numerous applications today. Its continued use has been ensured primarily due to the simplicity of its construction and other features such as durability, low maintenance, and good sound as well as thermal insulation properties [1]. Additionally, URM structures form a significant component of the existing building

Published online: 29 October 2024

stock in many regions, including countries with significant seismic activity [2]. It is also well known that traditional URM structures have a significant vulnerability under seismic actions. However, the majority of studies addressing this vulnerability have focused on the primary load transfer path of seismic forces in a URM structure, i.e., the in-plane direction of walls. Consequently, the out-of-plane (OOP) response of URM structures is still one of the most complex and poorly understood areas of seismic analysis. This is despite OOP failures being extensively reported by damage observations in the aftermath of recent and past earthquakes as an important cause of structural collapse [3–7]. When considering OOP failures, a distinction can be made between one-way bending of the wall, which occurs in walls without side supports (or in long walls, for whose central section the effect of side supports is negligible), and two-way bending in walls, which have at least one vertical and one horizontal edge supported. Among these two failure modes, one-way bending is distinctly more vulnerable compared with two-way bending, as evidenced by large-scale dynamic experimental campaigns [8]. This paper focuses exclusively on the more vulnerable one-way bending OOP response of URM walls.

Several experimental campaigns have been carried out to investigate the one-way bending OOP response of URM walls. These include, but are not limited to, the work by Griffith et al. [9] who tested four one-way spanning walls, subjecting them to both static as well as dynamic input. Simisir et al. [10] tested one-way spanning walls dynamically, taking into account the effects of flexible floor diaphragms. Advances in the shake table testing of one-way spanning walls have also been made by Penner and Elwood [11] and Giaretton et al. [12]. Messali et al. [13] tested two one-way bending walls under static loading. In this domain, certainly one of the most comprehensive investigations was carried out by Graziotti et al. [14] who performed incremental dynamic tests on four one-way spanning single leaf and cavity walls, which has been adopted as the reference experimental campaign in this paper. It is interesting to note that in these reference experiments [14] the aim was to achieve idealized conditions regarding support and loading. These conditions were chosen to be easily reproducible in numerical simulations rather than to represent the realistic conditions that one-way bending walls typically experience in actual buildings. However, it is well known that boundary conditions can significantly influence the OOP response of URM walls, and that walls in real-world buildings encounter much more complex scenarios compared to the idealized conditions considered in benchmark experiments. The effect of such complex dynamic boundary conditions on the OOP response of URM walls has also been experimentally documented to be significant in [8, 15–17]. The results suffer from the filtering and amplifying effects of the building structure in which the wall is located and are particularly influenced by the diaphragm response and the position of the wall within the structure. Such complex scenarios and their effects on the OOP response of walls are best analyzed using high-fidelity numerical models. Proper quantification of these effects can only be achieved by first calibrating the adopted modeling strategy against the benchmark experiments with idealized boundary conditions, and then applying more complex scenarios to the calibrated high-fidelity modeling strategies. This calibration poses several challenges, including defining an adequate modeling strategy, establishing a calibration procedure for material properties, determining appropriate damping, ensuring numerical stability with optimized computational effort, and accurately representing the boundary conditions.

This paper takes a step towards understanding the effects of such effects on the OOP one-way bending response of URM walls by initially focusing on the development and subsequent calibration of a high-fidelity numerical modelling approach against incremental dynamic experiments, as reported in Sects. 2 and 3 of the manuscript. A damaging block-based modelling strategy [18] is adopted towards this end, with the present work representing the first instance in which such a modelling strategy has been adopted for simulating the dynamic behavior of URM under multiple steps of sequential earthquake loading. An additional novelty is that damping governing the energy dissipation of the walls is introduced within the blocks, simulating the compressive crushing and tensile cracking of masonry units, rather than in the interface elements between these blocks, as is common practice. The calibrated numerical model developed through this process is optimized to require minimal computational effort while maintaining accuracy in simulating the experimental behavior measured in the benchmark experiments described in Sect. 4.

This calibrated and optimized numerical model is then used to provide preliminary understanding of the effect of a single dynamic boundary condition that all OOP walls are subjected to, i.e., the relative motion of top and bottom supports. This is achieved via a sensitivity study reported in Sect. 5. The primary variable considered in this sensitivity study is the amount of global structural damage accumulated from previous loading events, which indirectly determines an incremental difference in motion at the top and bottom supports of the analyzed wall. Particular attention is also given to exploring potential simplifications to capture the effect of such complex loading scenarios. These simplifications can be adopted for single-degree-of-freedom (SDOF) modeling approaches, which remain widely used and particularly attractive for the OOP seismic assessment of individual URM walls due to their minimal computational effort, especially for conducting large-scale seismic risk investigations. Concluding remarks are ultimately presented in Sect. 6.

2 Numerical modeling approach

This study adopts the block-based numerical model presented in [18], in which masonry is represented unit-by-unit in a three-dimensional framework, using zero-thickness mortar joints and expanded blocks. The zero-thickness joints, modeled using a contact algorithm with a master–slave formulation [19, 20], represent mortar layers. This approach, referred to also as meso-scale [21, 22] or simplified micro-scale [23, 24] modeling of masonry, has been extensively adopted in the literature [22, 25–28] for the high-fidelity study of material- to structural-level behaviors. It is preferred over more detailed approaches (such as in [29] where mortar is explicitly modeled) as it significantly reduces the number of active elements and degrees of freedom, which in return, lowers the computational efforts while maintaining a similar level of accuracy.

Initially developed for structural analyses in static and quasi-static conditions, the model has been adapted in this study to handle dynamic simulations. Specifically, a procedure for the simplified characterization of the mechanical behavior of the constituents is proposed in Sect. 2.1 to reduce computational burdens while maintaining a desired level of accuracy when analyzing walls. Moreover, the model is extended to dynamic analyses in Sect. 2.2 and the energy dissipation is accounted for through the incorporation of Rayleigh damping in the bulk, as explained in Sect. 2.3. The modeling strategy proposed herein is not only meant for the capturing of one-way bending out-of-plane behavior (presented in detail in the following sections), but also more complex in-plane and out-of-plane structural responses. Accordingly, it is presented in full with all constitutive behaviors required to simulate any possible outcomes in such analyses. This section describes only the new key features of the modeling approach. The reader is encouraged to refer to Appendix for more detailed information.

2.1 Nonlinear response of blocks and joints

The nonlinear response of expanded blocks is governed by the isotropic plastic-damage constitutive model developed in [30], also known as Concrete Damaged Plasticity (CDP) model. In uniaxial conditions, compressive crushing and tensile cracking of the bulk are assumed. The uniaxial stress–strain curves in compression and tension serve as primary input data for the CDP model, representing the crushing of the masonry assembly (wallets and walls) under uniaxial compression and the splitting of the units (referred to as bricks herein) under direct tension, respectively. The Drucker-Prager type multi-yield surface proposed in [31] characterize the strength domain under multiaxial stresses, projecting the uniaxial constitutive behavior into a three-dimensional space. Masonry joints are conceived with a non-dilatant nonlinear response which lump the behavior of both the unit-mortar interface and the mortar layer. They are based on the relative displacement of master surfaces and slave nodes, being the response cohesive in tension and cohesive-frictional in shear. The shear and tensile responses are coupled using the Mohr–Coulomb yield surface with tension cut-off.

To address the shortcoming of the high-fidelity models in their high computational demands when applied to walls and larger structures [32], this section proposes a simplified mechanical characterization of expanded blocks and the joints in order to increase the efficiency of the adopted modeling strategy. The mechanical characterization of the model proposed

herein, although partly similar to the previous works [18], is slightly more sophisticated and has not been proposed as a structured characterization methodology before. It is validated in previous works against small- to large-scale quasi-static cyclic and pushover experiments on masonry assemblages [33]. It is also shown in additional sensitivity studies to be simple enough significantly improve the performance of the model, while not being overly simplified to reduce the accuracy [33].

The monotonic tensile and compressive uniaxial behaviors of the expanded blocks are shown through red curves in Fig. 1a. Typically, the compressive response shows an elastic linear phase followed by a hardening and a subsequent softening phase. The tensile behavior shows an elastic response ensued by a softening branch [34]. However, given the variability of the experimental tests, a simplified setting of the mechanical behavior in expanded blocks is employed as shown in Fig. 1a. Specifically, in compressive regime, the pre-peak hardening behavior (proven to have significant influence on the computational demands [33]) is idealized by linear elastic behavior (with the elasticity modulus representative of the masonry Young's modulus in the vertical direction, E_m, according to [18])) ensued by a subsequent plateau equal to the maximum compressive strength of masonry (f_m') and defined over the strain interval

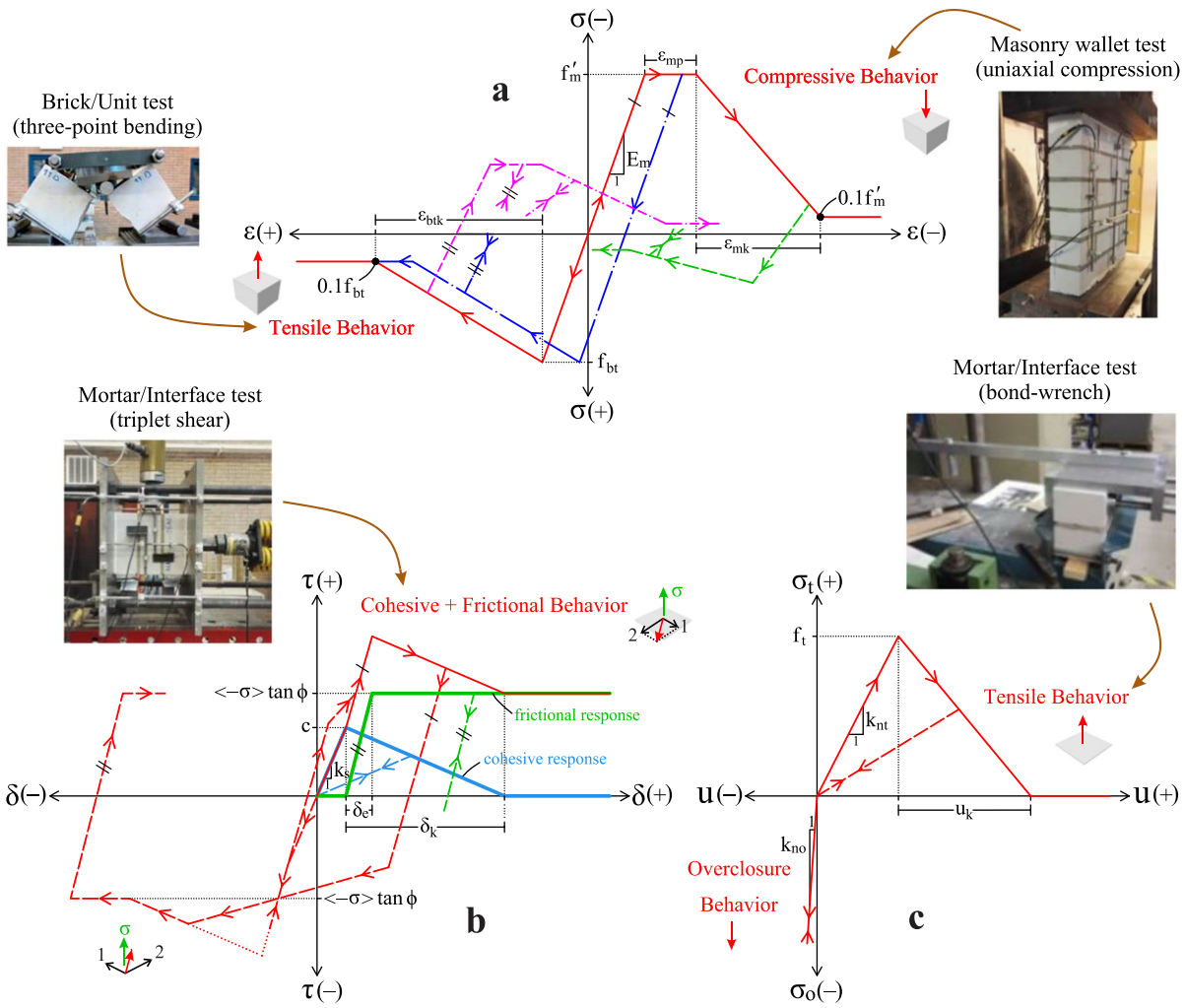

Fig. 1 Constitutive material behaviors considered in the numerical model: uniaxial compressive and tensile behaviors of the expanded blocks (**a**) and shear (**b**) and normal (**c**) behaviors of zero-thickness joints

ε_{mp}. The plateau is followed by linear softening until a strain value of ε_{mk}. Similarly, the tensile behavior is characterized by ε_{btk} linear softening function after the attainment of the maximum tensile strength (f_{bt}). Finally, a residual strength (10%) is here considered for both tensile and compressive regimes of the expanded blocks to avoid divergence issues during the simulations. The cyclic response shows a more complex behavior characterized by reduced-stiffness for unloading and reloading. As the figure exhibits, the stiffness remains unchanged in elastic phases and compressive plateau (dashed blue curve), but reduces during compressive and tensile softening proportionally to the loss of compressive and tensile strengths (dashed green and pink curves), respectively. No recovery is supposed for uniaxial compression-to-tension and tension-to-compression stress state transitions. In other words, the cyclic stiffness and strength of the tensile regime is affected by the compressive damage, and vice versa. Further details about the nonlinear response of the expanded blocks are collected in the Appendix 3.

In the joints, the behaviors shown in Fig. 1b and c are adopted. The shear- (blue curve, Fig. 1b) and tensile-cohesive (red curve, Fig. 1c) regimes are expressed via an initial elastic response and a subsequent softening phase. Since sensitivity studies showed a significant influence of the damaging behavior of the joints on the computational demands, simple linear softening responses are adopted [33]. The cohesive elastic response in normal and shear directions is characterized by k_{nt} and k_s stiffnesses, respectively. The peaks of the cohesive tensile and shear regimes are defined as f_t and c, respectively. Finally, the length of the softening regime is represented by u_k in tension and δ_k in shear. The shear-frictional response (green curve, Fig. 1b) is characterized by a constant friction angle (ϕ) and depends upon the applied vertical stress (σ). Using the elastic slip concept to combine shear-cohesive and shear-frictional responses, the frictional response is only activated upon the initiation of damage in cohesive response and after a frictional elastic slip (δ_e), which can be seen as a slip tolerance. The cyclic behaviors of the joints are characterized by reduced stiffness in the tensile- and shear-cohesive regimes proportional to the damage, while the shear-frictional response shows elastic loading–unloading-reloading independent from damage. The tensile- and shear-cohesive behaviors are coupled, meaning that damage in the former affects equivalently the latter, and vice versa. The shear response is assumed isotropic in the plane of the joint. Hence, it is expressed based on the vectorial summation of the shear stresses and relative displacements in longitudinal and transverse directions in the plane of the joint, shown in the figure with vectors 1 and 2, respectively. Finally, the joints show an elastic behavior with high stiffness (k_{no}) against compressive contact stresses to make negligible the compenetration of the blocks. Additional information regarding the behavior of the zero-thickness joints is presented in the Appendix 2.

2.2 Time integration

The gravity load and the additional vertical loads are applied on the wall in a nonlinear static analysis framework, as was previously used with the numerical approach in [18, 29]. For dynamic analysis, an implicit Hilbert-Hugh-Taylor (HHT) direct integration solver [35] with automatic time-stepping incrementation is used. The method, also known as the generalized HHT-α method, extends the Newmark family of integrators by improving second-order accuracy in low-frequency response and introducing numerical damping to control high-frequency noises. The numerical energy dissipation is controlled by the α_{HHT} parameter, where $\alpha_{HHT} = 0$ corresponds to no numerical damping and $\alpha_{HHT} = -0.5$ provides a maximum of 6% damping. It is noteworthy that increasing the numerical damping adversely affects the accuracy at low-frequency range. Hence, simulations adopting excessive numerical damping may show a different response as well as energy dissipation than the correct one [36]. In the case of this study, an $\alpha_{HHT} = -0.05$ is adopted in order to avoid such problems. This introduces a slight numerical damping (less than 1% of the total energy) to control the high-frequency noises while not altering the solution at lower frequencies.

The HHT solver uses the Newton Raphson (NR) iterative solution for nonlinear problems. The time-incrementation interval is scaled up and down based on the required number of NR iterations. In case of high nonlinearly, smaller intervals are used for better convergence. On the other hand, if the previous increments converge fast, the time increment is increased up to a maximum allowed value (Δt_{max}) for a quicker analysis. Previous works [37] show that Δt_{max} should

be specified with care as low values lead to unnecessarily high computational times and a large Δt_{max} may cause divergence issues in increments with high nonlinearity. The choice of Δt_{max} is also observed to affect the amount of numerical damping especially when it is more than 10% of the period of the first-mode period of the numerical model, which in return reduces the accuracy of the solution. As a rule of thumb and in accordance with the recommendation of Hassan [37], this study adopts a Δt_{max} equal to the time sampling interval of the instruments used in the experiments. This setting, together with the selected HHT parameters, introduces a very limited dissipation through the numerical integrator. It also allows for recording numerical data as frequently as in the experiment, enabling a one-to-one comparison of the outcomes. Additionally, it optimizes the computational time, as discussed for the case study in Sect. 4.

2.3 Damping model

The numerical model developed in [18] was limited to steady-state applications where the energy was dissipated only through static and quasi-static mechanisms such as the plasticity and damage of the blocks, frictional sliding and normal cracking of the zero-thickness joints, and hysteretic behaviors as formulated in Sect. 2.1. Hence, the model did not account for the kinematic energy dissipations in dynamic conditions due to the viscosity of the structure or the impact of different components. In other words, the model lacked a structural damping matrix to be used in the dynamic solver.

Different methods commonly used in the literature for the treatment of dynamic energy dissipations include introducing damping in the response of the joints or the blocks. The former is especially effective when simulating dry joint masonry structures under rocking motions. This is done by assigning the joints with an artificial viscous damping coefficient to simulate the energy dissipation during the impact of masonry units [38]. The damping coefficient can be calculated by defining a coefficient of restitution based on experimental data [39] or using the well-established classical rocking theory [40]. However, this approach is generally not sufficient to comprehensively represent the more complex behaviors in regular URM structures, wherein the energy is also dissipated through more complex phenomena and coefficient of restitution concept does not hold. In other words, the higher deformability of the units and mortar in regular URM leads to the dissipation of kinematic energy under velocity-dependent loadings, such as seismic actions, which cannot be reproduced solely by using damping in the joints. On the other hand, using more complex viscous damping models in regular non-dry zero-thickness joints is not possible as (coupled with the high elastic stiffness of the joints) they would significantly reduce the stable time increment size used by the solver. This, in turn, either causes divergence problems or significantly increases the computational time [20]. Hence, this study introduces viscous damping in the blocks in the form of Rayleigh damping to govern the dynamic energy dissipation.

Rayleigh damping assumes that the total damping of the structure can be represented by the effects from rigid-body motions and the internal deformations of the structure [41], via a mass-proportional (α_R coefficient) and a stiffness-proportional term (β_R coefficient), respectively. The merits of Rayleigh damping over other approaches can be explained by its easy implementation in numerical frameworks, straightforward calibration methodology, and acceptable performance in approximating the damping characteristics of many real-world structures without adding computational drawbacks [42]. Another advantage of using Rayleigh damping lies in the combination with the implicit HHT solver used in this study. While in previous implementations in explicit solvers, the stiffness proportional coefficient (β_R) is typically set to zero to avoid over-shrinking of the stable time increment, leading to increased computational burdens [43, 44], such simplification is not required when an implicit solver is used. Indeed, unconditionally stable implicit solvers (such as HHT) allows faster analyses [20]. Moreover, the stiffness of the expanded blocks is typically not high enough for the stiffness-proportional term to affect the time-stepping stability.

A commonly known drawback of Rayleigh damping is identified as the overdamping of low- and high-frequency responses outside the target frequency range caused by mass- and stiffness-proportional terms, respectively [45]. In linear simulations, this effect prevents a correct representation of damping response across all frequency ranges and outside the target deformation modes. This effect becomes even a more significant limitation in simulations of

specimens with geometrical and material nonlinearity. The propagation of damages and large deformations alter the stiffness of the specimens during the analysis, which in return changes the frequency range of interest for Rayleigh damping. Since the α_R and β_R coefficients remain constant mid-simulation, this effect will result in incorrect damping of the nonlinear responses, which leads to deviation from the expected behavior observed in the experiment. To sufficiently reduce the overdamping effects, it is recommended to select a target damping ratio (ζ_R) that remains feasible throughout the simulation of the specific structure under study. As such, the current study tackles this limitation by investigating the applicability of a range of target damping ratios including the values commonly reported for masonry structures (2% to 5%) [46]. Although the selection of the target damping ratio is problem-dependent, the sensitivity study performed here can provide an insight into what to expect when changing the damping ratio to lower or higher values.

3 Modeling incremental dynamic out-of-plane experiments on masonry walls

Incremental dynamic experiments subjecting unreinforced masonry walls to out-of-plane seismic actions carried out by Graziotti et al. [14] at EUCENTRE Foundation in Pavia, Italy are simulated to test the proposed modeling strategy and investigate the effects of damping models on numerical results. The campaign comprehensively studied masonry at different levels, from material-level characterization to building-level dynamic shake table tests. Within the campaign, several tests were performed on single-leaf and cavity walls with different geometries under dynamic out-of-plane shake table loading in two-way and one-way bending configurations. For the purposes of the current study, the test on a single-leaf one-way bending calcium silicate wall is simulated. This section provides an overview of the specimen, the testing procedure, and the outcomes of simulating the wall via the proposed modeling strategy.

3.1 Experimental benchmark

The wall (indicated as SIN-03–00/SIN-01–00 in the reference publication [14]) is shown in Fig. 2a and was 2754 mm high and 1438 mm long. It was constructed with 34 rows of 212×71×102 mm (length×height×thickness) calcium silicate bricks and multipurpose M5 mortar in a running bond configuration and 10 mm mortar layers. The test setup, shown in Fig. 2b, was designed to apply an equal load to the top and bottom of the wall. The base of the wall was placed on a regular mortar bed joint and rested on a prestressed reinforced concrete foundation fixed to the shake table via steel bolts. A rigid steel frame transferred the dynamic motion of the shake table to the top of the wall with minor amplification and imposed it on the wall via a steel beam, as shown in Fig. 2c. The beam was placed on the top of the wall and enclosed the last brick row via L-shape profiles. A pinned connection is considered between the frame and the beam, which allows uplift and rotation around the in-plane axis at the top of the wall. The vertical bracing spring system of Fig. 2d applied and maintained an almost constant compressive force at the top of the wall, using low-stiffness springs that resulted in a maximum of 5% variation in the applied vertical force.

The specimen was subjected to multiple steps (herein referred to as runs) of consecutive dynamic loading with the sequence reported in Table 1. The acceleration time histories shown in Fig. 3a were used at different runs as the input motions for the shake table. The Gr-1 signal represents the dynamic motion expected at the ground level due to induced seismicity in the Groningen area of the Netherlands at the time the experiments were carried out, and the Gr-2 record is the first-floor motion recorded from the numerical model of a two-story building subjected to Gr-1 at its base. The third accelerogram is a 2 Hz Mexican hat pulse known as Ricker Wavelet, or RWA for short. The spectral acceleration data of the input motions is shown in Fig. 3b. While the input motions shown here represent the signals at 100% of their original amplitude, it should be noted that the test was conducted in an incremental dynamic manner, where the loading amplitude was scaled to different levels at different runs, and was increased until the specimen collapses. This means that the specimen was affected by all damages accumulated from preceding loading runs, similar to real-world structures where the walls can be potentially pre-damaged from previous loading events during the lifetime of the structure. According to Table 1, the specimen was first

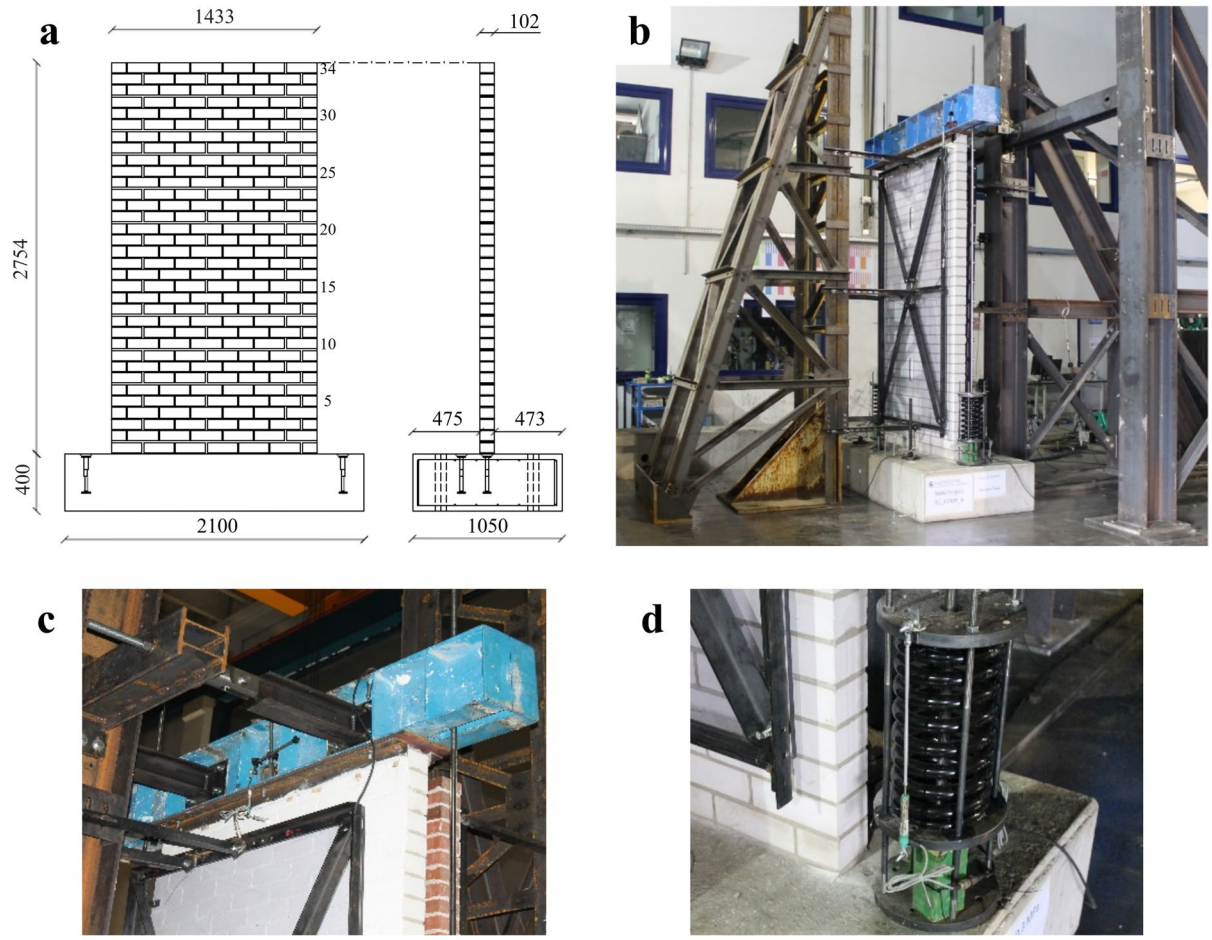

Fig. 2 Geometry and experimental setup of the one-way-bending benchmark experiment wall [47]: Dimensions in millimeters (**a**), test set-up (**b**), top beam (**c**), and vertical loading system (**d**)

subjected to 9 runs of Gr-1 loading and four runs of RWA pulse under 0.3 MPa pre-compression. Afterward, the pre-compression was reduced to 0.1 MPa, and the wall was subjected to another series of out-of-plane loading consisting of eight runs with Gr-1, four with RWA, and three with Gr-2. It should be noted that the loading runs were performed one immediately after another without bringing the specimen back to its original resting position (zero-displacement condition). The sign of the peak table accelerations indicates the direction of the load application, meaning that the signal of RWA runs is applied in an opposite direction with respect to Gr-1 and Gr-2 signal. In addition to the dynamic runs, a white noise (indicated with WN) excitation was applied after the application and reduction of the vertical load for dynamic identification of the natural deformation modes and frequencies of the specimen in the out-of-plane direction.

3.2 Numerical model set-up

The values listed in Table 2 are used to characterize the mechanical behavior of joints and blocks as described in Sect. 2.1 and shown in Fig. 1. The model mechanical characterization has been conducted according to [18], where the outcomes of small-scale experimental tests were directly used to define the model input parameters, leading to a sufficiently accurate estimation of the response at the wall-scale level. In other words, the reported values are obtained directly from simulating reference small-scale tests

Table 1 Loading sequence adopted in the testing of the experimental benchmark [14]

0.3 MPa vertical compression applied				vertical compression reduced to 0.1 MPa			
Run #	Input	Scale	PTA* [g]	Run #	Input	Scale	PTA [g]
0–1	WN	–	–	0–2	WN	–	–
1	Gr-1	20%	+0.04	14	Gr-1	40%	+0.08
2	Gr-1	40%	+0.09	15	Gr-1	80%	+0.17
3	Gr-1	80%	+0.16	16	Gr-1	100%	+0.21
4	Gr-1	100%	+0.20	17	Gr-1	160%	+0.34
5	Gr-1	160%	+0.32	18	Gr-1	200%	+0.41
6	Gr-1	200%	+0.42	19	Gr-1	250%	+0.51
7	Gr-1	250%	+0.52	20	Gr-1	300%	+0.60
8	Gr-1	350%	+0.74	21	Gr-1	350%	+0.73
9	Gr-1	450%	+0.96	22	RWA	100%	−0.26
10	RWA	400%	−1.11	23	RWA	200%	−0.48
11	RWA	600%	−1.63	24	RWA	300%	−0.72
12	RWA	400%	−1.05	25	RWA	300%	−0.96
13	RWA	600%	−1.88	26	Gr-2	100%	+0.44
				27	Gr-2	150%	+0.64
				28	Gr-2	200%	+0.85

*Recorded peak table acceleration

within the experimental campaign, performed on the same materials used to construct the wall specimen reported in [47], and are then used as input for wall-scale simulations. This approach allows for a robust characterization of the mechanical behaviors by adopting reasonable input values that fall within the reported variation range of the material properties from the benchmark campaign. More information regarding the verification of this approach against quasi-static wall- and structural-level experiments can be found in [18, 29].

The uniaxial compression test on masonry wallets and three-point bending tests performed on calcium silicate bricks are used to calibrate the compressive and tensile behaviors in the expanded blocks, respectively. The former is also employed to obtain the overclosure stiffness of the joints (k_{no}). The default dilatancy angle and CDP parameters considered for quasi-brittle material such as masonry are used. The shape of the Drucker-Prager type multi-yield surface [30, 48, 49] is characterized by 0.1 eccentricity (∈), 1.16 as the ratio between the biaxial and uniaxial initial compressive strengths (f_{b0} and f_{c0}, respectively), and 2/3 for the ratio of the second stress invariant in tensile meridian to the second stress invariant in compressive meridian (ρ). In addition, a 10˚dilatancy angle (ψ) is assumed based on previous experimental and numerical studies [50, 51]. Similarly, a 0.17 Poisson's ratio (ν_m) is assumed for the expanded blocks according to typical values reported for masonry [34]. The tensile-cohesive strength of the joints (f_t) is obtained from the bond-wrench flexural test, and shear-cohesive as well as shear-frictional behaviors are calculated from triplet shear tests. For simplicity, the length of tensile- and shear- cohesive softening regimes are here assumed to be equal in magnitude (i.e. $u_k = \delta_k$). Finally, similar properties are assigned to the head and bed joints and no distinction is made between the behavior of the two.

The geometry of the studied wall is generated using 222×81×102 mm (length×height×thickness) expanded blocks, resulting in a numerical representation with length and height identical to the original specimen. Although great care is necessary in simulating the boundary conditions adopted in experiments conducted at wall scale, a certain level of idealization is applied to avoid unreasonable computational time. For instance, the boundary conditions and loads are applied directly to the extremities of the specimen instead of simulating the loading frames and instruments, as shown in Fig. 4. Previous studies have confirmed the validity of this approach, even for capturing complex out-of-plane response [18, 26, 29]. The numerical wall is placed on a semi-rigid (in fact, elastic with high stiffness) foundation, on which the out-of-plane motion is imposed in terms

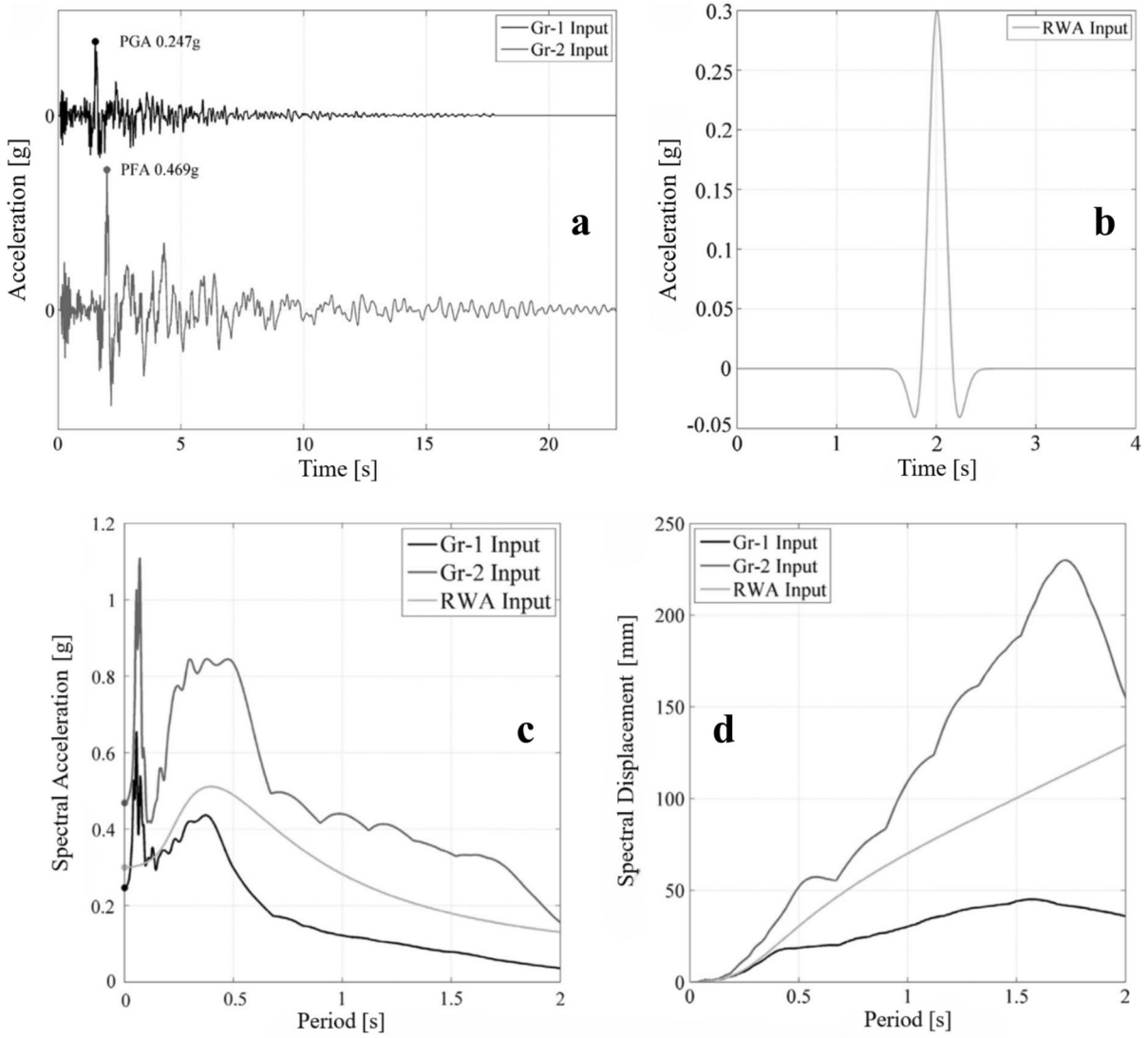

Fig. 3 Overview of the loading input signals used in the testing of the experimental benchmark [14]: acceleration time histories of Gr-1 and Gr-2 (**a**) and RWA (**b**) input motions, and 5%-damped acceleration (**c**) and displacement (**d**) spectrums of the signals

of acceleration time history. Regular mortar properties are assigned to the lowermost bed joint. At the top of the wall, the out-of-plane acceleration, vertical overload, and boundary conditions are imposed to a reference point. The top surface of the wall is then tied to the reference point through kinematic coupling. The wall is assembled in the x–y plane, and the out-of-plane direction is aligned with the z-axis. In accordance with the experiment, all degrees of freedom, except vertical translation and rotation about the x-axis, are restricted at the reference point.

The complete loading sequence reported in Table 1 is considered in the simulation. Moreover, the entire time-history of the loading signal in each run is applied to the numerical specimen. Although this might increase the computational time. The low-amplitude motions before the major excitation part might cause micro-damages and alter the behavior under higher-intensity portions. On top of that, the low-amplitude resting portion after the major-excitation part allows the higher-frequency loadings to propagate through the specimen and amplify the

Table 2 Model mechanical characterization

Expanded blocks							
Elastic behavior		CDP parameters		Compressive behavior		Tensile behavior	
E_m[MPa]	3236.0	ψ[°]	10	f_m'[MPa]	6.3	f_{bt}[MPa]	1.5
ν_m[−]	0.17	ϵ[−]	0.1	ε_{mp}[−]	0.006	ε_{btk}[−]	0.002
Density [kg/m^3]	1852.0	f_{b0}/f_{c0}[−]	1.16	ε_{mk}[−]	0.010		
		ρ[−]	2/3				
Zero-thickness joints							
Overclosure behavior		Tensile cohesive behavior		Shear cohesive behavior		Shear frictional behavior	
K_{no}[N/mm^3]	241.4	k_{nt}[N/mm^3]	241.4	k_s[N/mm^3]	103.1	tan ϕ[−]	0.42
		f_t[MPa]	0.16	c [MPa]	0.21	δ_e[mm]	0.001
		u_k[mm]	0.4	δ_k[mm]	0.4		

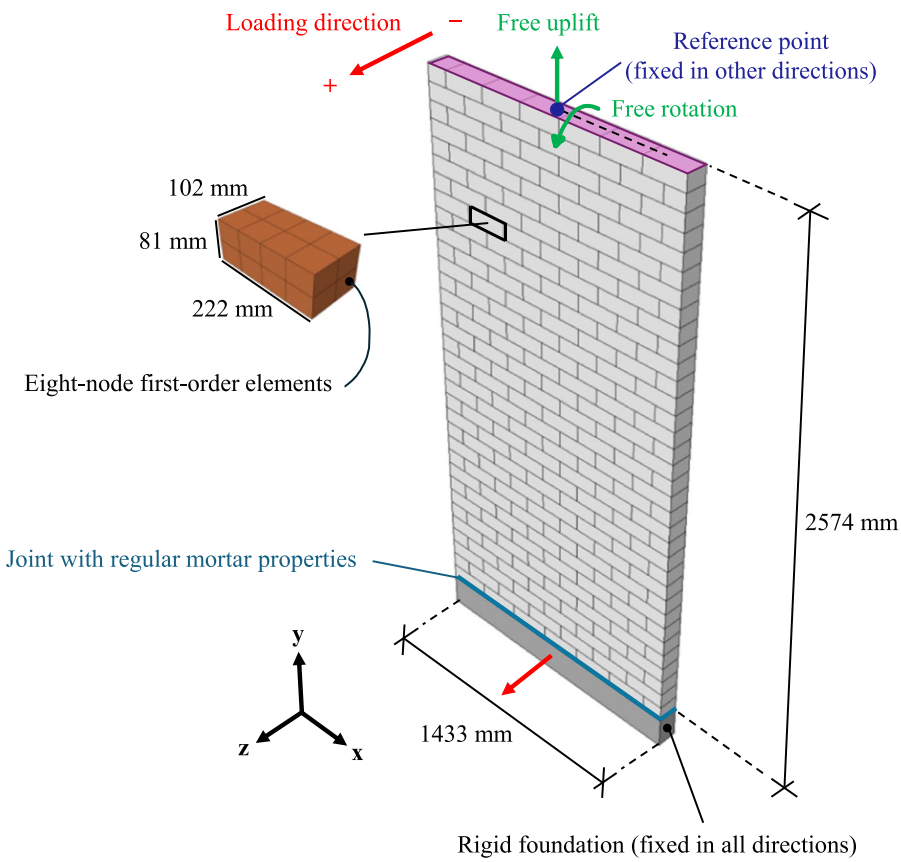

Fig. 4 Geometry, mesh discretization, and boundary conditions assumed to simulate the dynamic experiment

damages. Only the white noise runs are skipped to reduce the computational time, as they do not affect the behavior.

The simulation of dynamic behavior poses a challenge in reproducing the same motions experienced at the boundaries of the specimens. Loading devices, such as shake tables, rarely perfectly recreate the intended input motion, and often over- or undershoot the imposed motion [52]. Moreover, the applied motion usually undergoes some changes

when transferred to the specimen, due to the uncontrolled amplification resulting from the loading apparatus [53]. Hence, this study uses the accelerations "recorded" at the base of the wall during dynamic loading to excite the numerical counterpart. This allows simulating the response under the experienced motions and to account for the uncertainties regarding the discrepancies between actual and theoretical motions to a great extent. Specifically, the same accelerations are used to excite both the top and bottom boundaries.

A downside of using the recordings of dynamic tests is the electrical noise inherent to experimental data collection devices, such as accelerometers. This requires cleaning the collected data using appropriate filtering techniques, such as those proposed by Boore et al. [54]. The filtering method may change from experiment to experiment based on the governed conditions and the quality of the sensors. In the case of this study, a fourth-order Butterworth bandpass filtering between the 0.1 to 50 Hz frequency range is applied to the recorded data to clean electrical noises imposed by the sensors [54].

The maximum time-stepping increment (Δt_{max}) is limited to 0.00391 s, which is the sampling rate of the accelerometers used in the experiment. After each loading step, including the dynamic runs and the placement and change of vertical pre-compression, frequency analyses are carried out to track the changes in the stiffness of the wall, which in return enables identifying the occurrence or accumulation of damages. Nonetheless, for the 1WB wall, the change in frequency is not significant up to the run at which collapse occurs. Regarding the Rayleigh damping in the blocks, it was decided to calculate the input coefficient based on the natural frequencies of the first and second out-of-plane deformation modes of the pristine numerical specimen under self-weight (12.09 Hz and 38.89 Hz for the single- and double-curvature mode, respectively). The adopted start and end frequencies accommodate the proper damping of the response over a wide frequency range. Moreover, the range excludes the higher deformation modes which were deemed to influence the response according to their low participating masses. In line with the discussion made in Sect. 2.3 regarding the limitation of Rayleigh damping in nonlinear simulations, different damping ratios (ζ_R) ranging from 0 to 8% are considered, and the simulation is conducted once for each of the adopted damping ratios. Assuming that the numerical specimen conforms with the experimental wall in all other aspects (material behaviors, boundary conditions, and loading), this sensitivity analysis allows the selection of the ζ_R best representing the specific case under study. It is noteworthy that the ratio of the adopted Δt_{max} to the lowest important natural period of the structure (0.0257 s, belonging to the double-curvature out-of-plane deformation mode) is 15%. This limits the numerical damping effects at this period and those of the lower deformation modes to less than 0.5%, limiting its effect on the accuracy of the response.

3.3 Simulation results

This section presents the outcomes of the numerical simulations and compares them to the results of the benchmark experiment. The maximum out-of-plane accelerations and displacements recorded at the mid-height of the specimen during each dynamic loading run are shown in Fig. 5, along with the total energy dissipated by the end of each run. The latter is calculated as the cumulative summation of the area enclosed inside the force–displacement response of the specimens during each loading run. The experimental results are shown with the solid black curves, while the colored, styled curves represent the results of the analyses conducted using different damping ratios in the expanded blocks. The collapse of the specimen during the experiment (run 28) and numerical simulations is highlighted with a cross (×) mark. The same indicator is used to identify the collapse of the numerical simulations. Where the collapse points of several specimens coincide, plus mark (+) is used instead of cross to highlight each collapse point more clearly. Several remarks can be drafted based on this figure, as outlined in the following. Firstly, even the smallest level of damping (2%) leads to a much more realistic simulation compared to when no damping is considered, since the 0%-damped model shows significantly higher displacements and accelerations compared to the other simulations and collapses at an early stage (run 11 instead of 28).

Secondly, the damping ratio value equal to 2% is observed to be still insufficient for regularizing the response, since the model shows relatively large noises in the accelerations during low-amplitude loading runs. Although the maximum acceleration

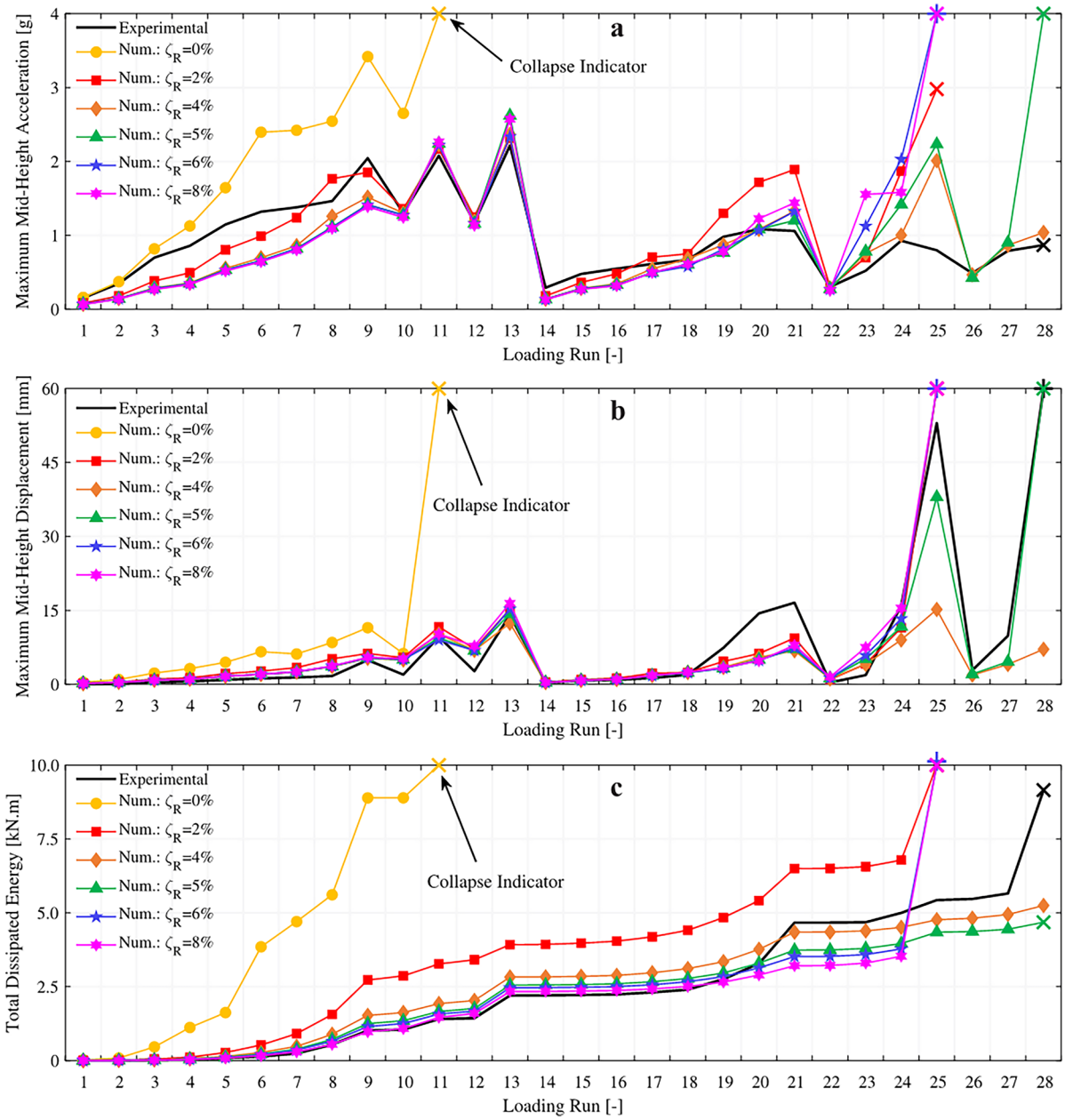

Fig. 5 Outcomes numerical simulation of the benchmark experiment using different damping ratios: maximum mid-heigh acceleration (**a**) and displacement (**b**) and cumulative energy dissipation (**c**) at each loading run

demands of the 2%-damped model during loading runs 1 to 9 appear closer to the experimental data compared to those of the other models in Fig. 5a, they are not part of the real behavior of the model but rather are caused to a great extent by the high-frequency noises recorded in the numerical response. As an example, a portion of the non-filtered time history of the mid-height acceleration during loading run 7 obtained from 2%-, 4%-, and 5%-damped models is shown in Fig. 6. The noises in the tail of the response in the 2%-damped model spike to 1.24 g, which is 55% larger than the peak acceleration experienced during the high-amplitude portion of the run (0.8 g). Conversely, the

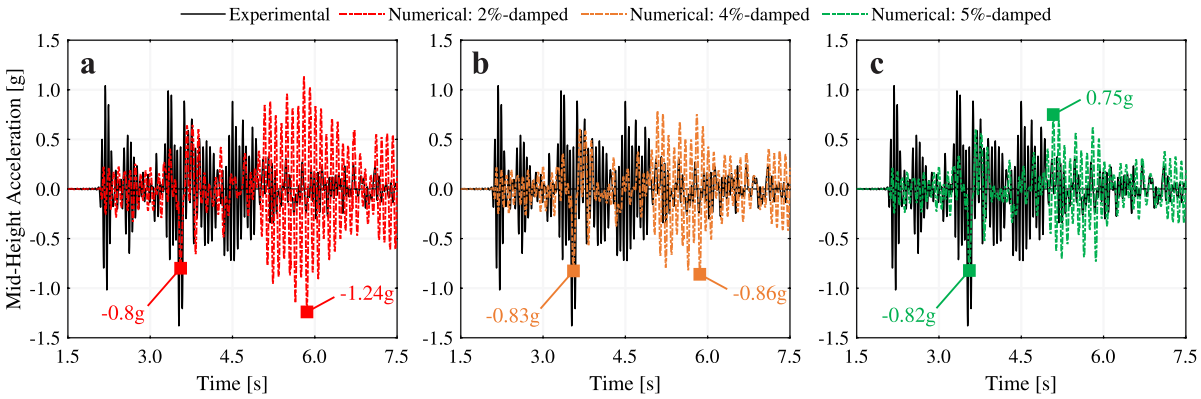

Fig. 6 Performance of simulations with different damping ratios against high-frequency noises: mid-heigh acceleration time-histories of 2% (**a**), 4% (**b**), and 5% (**c**) damped models during loading run 7

use of 4% and 5% damping controls the noises relatively better, as the spikes reduce to 92% of the peak response (0.75 g compared to 0.82 g) in the latter. The insufficiency of 2% damping ratio for the case of this study is also evident in its cumulative energy dissipation not being close enough to the experimental curve.

Thirdly, the selection of larger damping ratios, although leading to energy dissipations similar to the experiment, changes the loading step at which the wall collapses, with no observable pattern for this effect. For instance, the 4%-damped model remains stable, and the wall does not collapse throughout the simulation, despite its energy dissipation conforming with the experiment. Whereas, the 6%- and 8%-damped wall models collapse earlier than expected (loading run 25 instead of 28). Finally, for the case of this study case, the 5%-damped model shows the closest maximum mid-height displacements to the experiments and the wall collapses at the experimental loading run (28). As commonly accepted in the literature, 5% damping can lead to an acceptable estimation of the real-world response of the structures. Furthermore, Graziotti et al. [14] also confirm that the benchmark specimen has also shown between 5 to 10% damping during the pulse loading runs. Accordingly, the choice of using 5% damping appears a good compromise and is used in the following simulations. The large difference between the incremental energy dissipation of the 5% damped model with that of the experiment in loading runs 21 and 28 is explained in Sect. 4.

Figure 7 compares the failure mechanism of the numerical specimens with that observed in the experiment. All models show a one-way bending collapse similar to the experiments, with slight mismatches in the details. In all cases, a horizontal opening at the base joint (row 0) is obtained, as in the experiment. Then, the horizontal opening of the joint at the mid-height of the numerical specimens occurs one row above the position of the experimental crack, independently from the damping ratio considered. The horizontal cracking beneath the topmost brick row in the test is not explicitly gathered in the simulations, given the simplified boundary conditions adopted in the top surface. Indeed, the occurrence of the top crack is implicitly taken into account by considering free rotation at the top of the numerical specimen and not simulating the contact between the top beam and the wall, i.e., assuming that a crack will occur at the topmost horizontal mortar joint and the top can freely rotate afterward. Finally, the blocks do not show nonlinear behaviors since, similar to the experimental case, the damages are mainly concentrated in the horizontal mortar joints. This may cast doubt on the appropriateness of the complex nonlinear behaviors considered for the expanded blocks, described in Sect. 2.1. In other words, it may appear that the same outcomes could have been achieved by adopting linear elastic blocks and considering only the material nonlinearity of the zero-thickness joints. However, it should be noted that the modeling approach presented in this paper is not meant to be limited to one-way bending cases with only joint failures. On

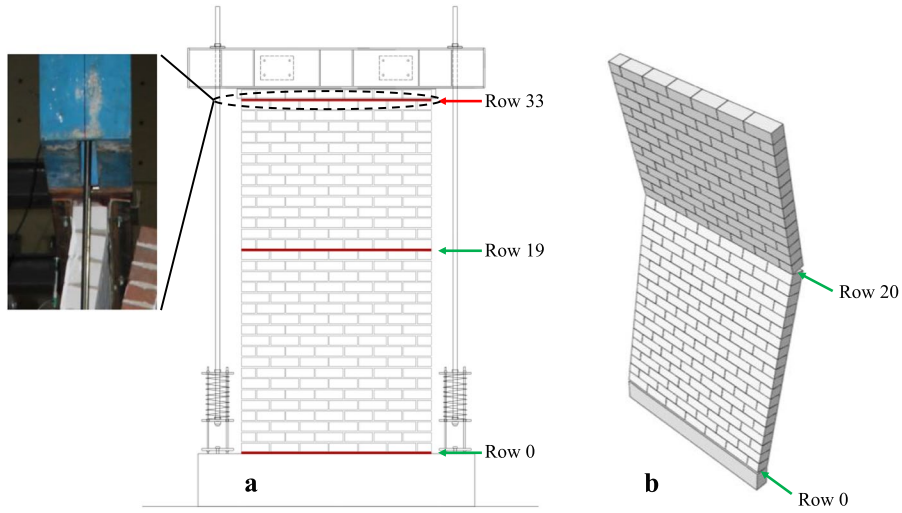

Fig. 7 Failure mechanism of the numerical simulations with different damping ratios: experimental (**a**) and numerical (**b**) crack patterns

the opposite, it is intended for broader structural applications with more complex behaviors and failure mechanisms. Moreover, the verified numerical model from this study has been used in a parametric study, explained in Sect. 5, which required to maintain the ability of capturing any type of failure mechanism. Hence, it is kept more general to be able to simulate all possible responses therein and any future studies.

4 Optimization of the computational effort for one-way bending out-of-plane dynamic simulations

Although the numerical model shows satisfactory results regarding failure mechanism and time-history responses, it demonstrates significant constraints in terms of computational demand. The simulation of the specimen under the complete loading sequence requires 137 h of analysis time (an average of 4.9 h per loading run) on relatively powerful hardware (16 CPU cores @ 4.2 Hz clock speed). Meanwhile, it is observed that considering the simulation of one-way bending behaviors, simplifying the geometry and the loading sequence, and using a larger time-stepping increment can reliably reduce the computational costs while maintaining the level of accuracy in the results [15]. This section explains how such procedures are implemented to decrease the complexity of the 5%-damped model (reference model) and its associated computational effort.

An investigation is carried out on the possibility of replacing the geometry of the numerical specimen with a representative shorter stripe to reduce the number of degrees of freedom and active contact definitions in the model, leading to fewer calculations per time-step increment. A sensitivity study is done by adopting four different geometrical variations with the same height as the original wall but different numbers of bricks per row, from one to two-and-half bricks. Table 3 shows the frequencies and deformation modes of the simplified models and the complete

Table 3 Frequencies of the original and simplified numerical specimens under self-weight load [Hz]

Mode	Full wall		2.5-Brick stripe		2-Brick stripe		1.5-Brick stripe		1-Brick stripe	
1	**OOP (1st)**	**12.09**	**OOP (1st)**	**12.08**	**OOP (1st)**	**12.07**	**OOP (1st)**	**12.06**	**OOP (1st)**	**12.05**
2	Torsion (1st)	28.87	**OOP (2nd)**	**38.83**	**OOP (2nd)**	**38.81**	**OOP (2nd)**	**38.79**	IP (1st)	35.37
3	**OOP (2nd)**	**38.89**	Torsion (1st)	57.03	IP (1st)	64.10	IP (1st)	50.70	**OOP (2nd)**	**38.74**
4	Torsion (2nd)	64.85	IP (1st)	75.34	Torsion (1st)	67.27	**OOP (3rd)**	**79.96**	**OOP (3rd)**	**79.84**
5	**OOP (3rd)**	**80.17**	**OOP (3rd)**	**80.05**	**OOP (3rd)**	**80.01**	Torsion (1st)	82.21	IP (2nd)	**93.28**

IP, in-plane; OOP, out-of-plane

specimen. It is demonstrated that such simplifications of the geometry, although introducing new in-plane deformation modes in the response, do not alter the natural frequencies and types of out-of-plane deformation modes. As highlighted in bold in Table 3, all numerical models exhibit similar out-of-plane modes of deformations and frequencies. Hence, the Rayleigh damping of the expanded blocks does not require recalibration. Moreover, when the rest of the settings (material, solver, damping, and constraints) are unchanged with respect to the original model, the simplified variations show failure mechanisms very similar to those of the reference numerical specimen. However, a slight difference was observed in the 2.5- and 2-brick stripe specimens, where the mid-height crack was developed one row below the other specimens (row 19 instead of 20), as shown in Fig. 8, consistently to the experimental observation.

Figure 9 compares the outcomes of the simulations on simplified models and the original numerical specimen in terms of maximum mid-height displacements and accelerations per loading run and force–displacement response. All models show similar failure patterns and responses to the full-wall model, except for the one-brick stripe, which collapses earlier (run 25 instead of 28), possibly due to not representing the typology of the wall (because of the absence of head joints). Moreover, the excessive slenderness of this variation and the introduction of the in-plane deformation mode (inside the damped frequency range) with a frequency close to the second out-of-plane deformation mode (35.37 Hz compared to 38.74 Hz), as indicated in Table 3, might have also contributed to the early collapse. Among the rest, the 1.5-brick stripe shows an adequately similar match to the reference model in maximum displacements and accelerations and the hysteretic response. This variation also shows a 76% reduction in the computational demands compared to the original model. It progresses through the complete loading sequence in 32.2 h (an average of 1.15 h per loading run) on the previously introduced hardware. Hence, this model was selected as the best substitution for the reference numerical specimen to reproduce the experimental outcomes with excellent accuracy and efficiency.

Finally, Fig. 10a compares the acceleration and displacement response of the 1.5-brick stripe and the original 5%-damped numerical specimen. The time history of the mid-height out-of-plane acceleration and displacement in the numerical analysis during the pulse loading in run 13 shows an excellent match and agreeable comparison with the experimental behavior. The hysteretic force–displacement responses of both simulations under the complete loading sequence are shown in Fig. 10b. The reaction forces of the experimental specimen are calculated by dividing the wall into two portions, one above and one below the mid-height,

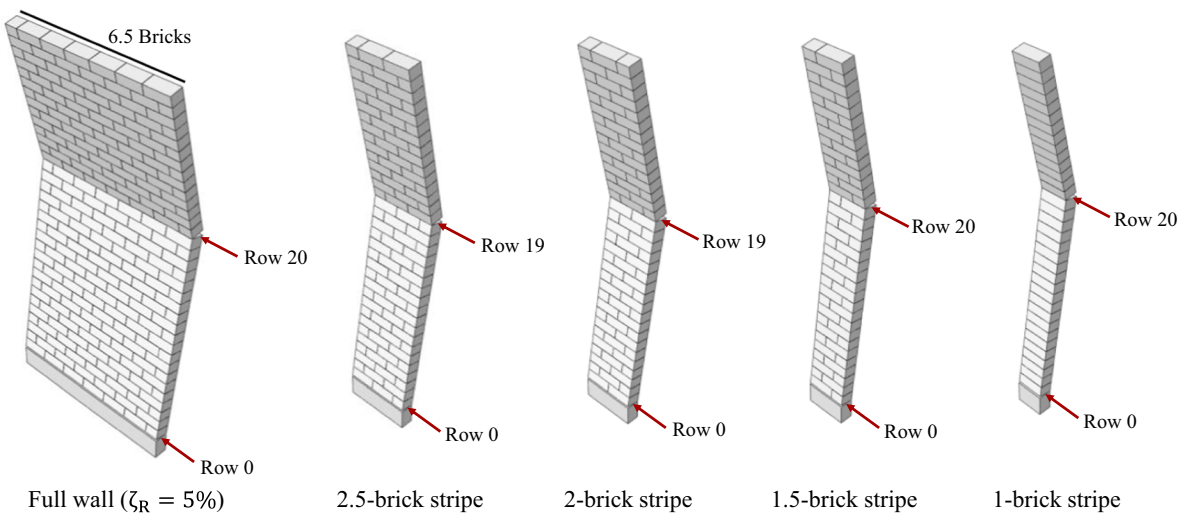

Fig. 8 Failure mechanism of the reference numerical specimen and the simplified variations

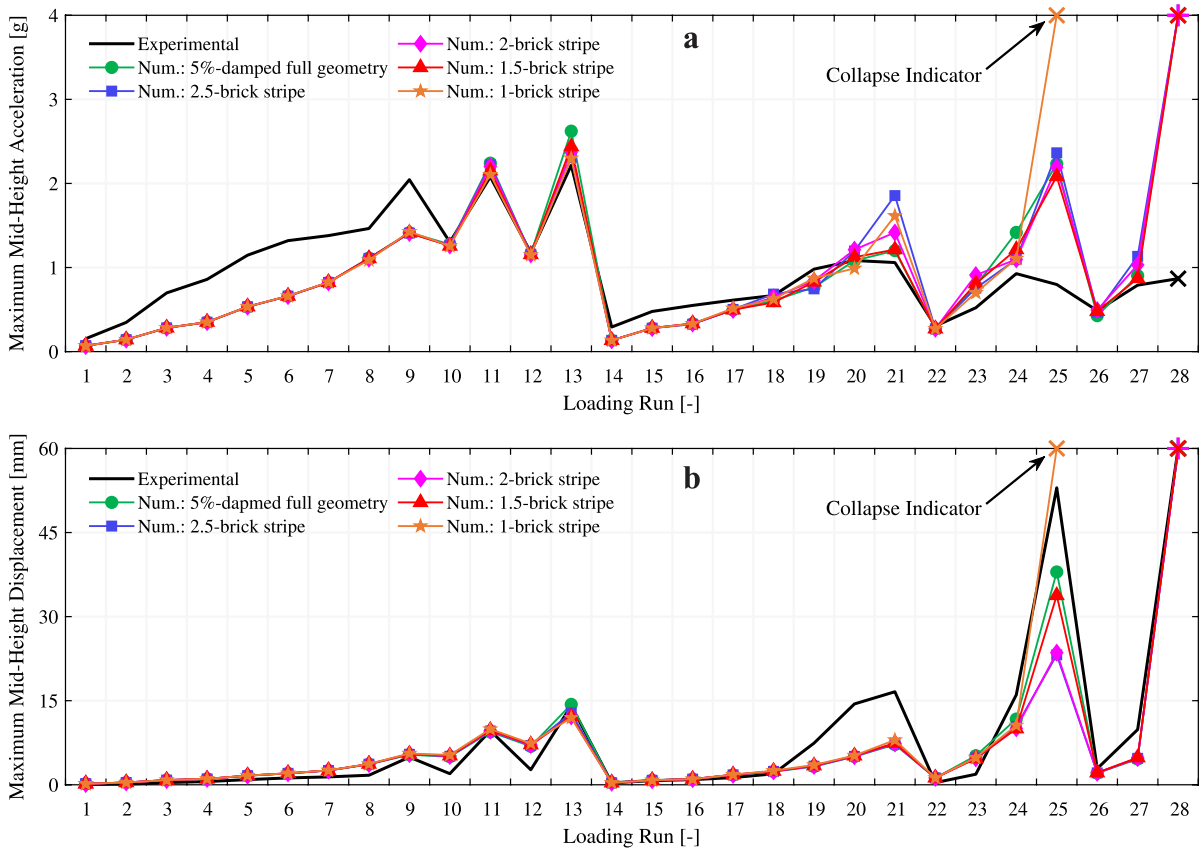

Fig. 9 Outcomes of numerical simulations with simplified geometries: maximum mid-heigh acceleration (**a**) and displacement (**b**) experienced during each loading run

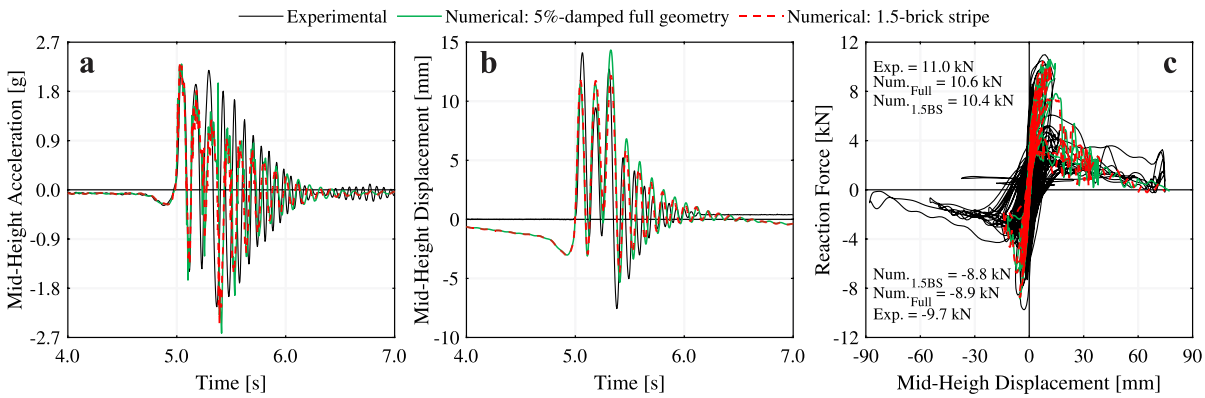

Fig. 10 Comparison of the response of full-geometry and 1.5-brick stripe numerical specimens: mid-height acceleration (**a**) and displacement (**b**) of loading run 13, and force–displacement response (**c**)

calculating the relative acceleration at the center-of-mass of each portion (assuming a triangular distribution of the mid-height acceleration over the height) and multiplying those accelerations by the mass of their corresponding wall portion. The numerical reaction forces are directly collected

from their base and top reference point. It should be noted that the reaction forces of the 1.5-brick stripe are scaled up by a factor of 6.5/1.5 to account for the difference in its mass with respect to the full-geometry specimens. Again, both numerical curves show good agreement with the experimental response. They show peak shear resistances only slightly lower than the experimental benchmark with 5% difference in the positive regime and 10% in the reverse direction. Moreover, both numerical models collapse at a maximum 74 mm mid-height displacement similar to the experimental wall.

Lower energy dissipation in the numerical simulations should be noted, specifically in loading runs 21 and 28. One possible reason for this effect, also noticeable in Fig. 5c for the full-wall model, might be overdamping of the damaged response because of using Rayleigh damping, as discussed in Sect. 2.3. Additionally, the reason may stem from the experimental conditions of the benchmark test. In loading run 28, relative slipping of the bricks above and below the cracked joints is inferred from the hysteretic response. However, such sliding is not observed in the numerical simulations. The outcomes of the simulations are consistent with the adopted constitutive model and the stress state at the moment of maximum opening of the flexural crack, since the large shear stresses remain well below the shear resistance, which benefits from the large compressive normal stresses determined by the section spatialization. However, both normal and shear stresses are computed by assuming one-fourth of the cross-section to be in compression, while a shorter length is observed during the test. This would result in higher stresses, potentially leading to a stress state where the actual shear strength is lower than that predicted by the Mohr–Coulomb yield surface. This effect may be further amplified by the imperfections in the specimens that could determine an additional stress localization. While the use of a finer mesh may allow for a more accurate definition of the compressive stress over the uncracked section, sliding at the brick–mortar interface of a largely cracked section would still remain difficult to predict. For this reason, a user might consider manually reducing the shear strength parameters in the case that such mechanism is deemed to be relevant. However, in the specific case considered in this study, since the minor sliding observed during the test had no major effect on the global response of the wall, no further efforts were made to capture it. In addition, such problem-specific micro-adjustment was also deemed inconsistent with the proposed general modeling procedure.

Another note should be made on the displacement capacity of the numerical models in the reverse direction being significantly lower than the tested wall (13 mm compared to 87 mm). Specifically, while the experimental specimen shows cyclic motions to large positive and negative displacements in the last loading run, the numerical wall collapses immediately after the first high-displacement motion. The high-intensity motions in the last loading run cause the complete opening of the boundary and mid-height joints, which lead to the complete loss of strength at those joints and to the collapse of the wall. Once again, adopting a finer discretization in the thickness direction might allow the model to recover stability by maintaining contact at more points. However, such investigation was not performed as increasing the number of elements would have resulted in an increased computational demand inconsistent with the adopted modeling approach. Moreover, since the maximum mid-height displacements of the models and the experiment were already similar and indicators of collapse conditions, no further attempts were made to refine the post-collapse behavior of the numerical walls.

Finally, regarding the elastic behavior, despite both the predicted wall response under the pulse load and initial wall stiffness being similar to the experimental outcome, the numerical model shows a 63% lower first natural frequency under 0.3 MPa vertical compression (11.83 Hz compared to 18.75 Hz). Moreover, while the natural frequency of the benchmark experiment drops to 14.27 Hz after the reduction of pre-compression to 0.1 MPa, the frequency of its numerical counterpart slightly increases to 12.00 Hz. This is justified by the uncertainties governing the experimental studies and the noises of the acceleration recordings used for experimental modal identifications.

The simulation time of the 1.5-brick stripe was further reduced to 13.9 h by removing the low amplitude loading runs (1 to 7 and 14 to 19), during which the specimen showed a purely elastic response. This resulted in an additional 13% reduction in simulation time without any change in the obtained response, reaching 89% lower computational

demands compared to the complete wall model. To understand the effects of time-stepping increments on the computational time, additional simulations were performed for the 1.5-brick stripe, adopting two to ten times larger maximum allowed increment sizes. It was observed that in the case of this study, although showing improved progression during low-amplitude loading runs by passing the increments with linear behavior faster, the new simulations required more iterations in nonlinear increments and showed convergence problems in high-amplitude runs. This resulted in 30% slower performance than the simulation with the original 0.00391 s time-stepping size. Moreover, increasing the increment size and moving away from stable values introduced artificial damping in the response through the HHT integrator [20]. This, in return, destabilized the dissipation through Rayleigh damping and caused early collapse for the numerical specimen case studied in this paper. Hence, the original time-step size was maintained. The results of the simulations with the simplified loading sequence and the larger time-stepping increments are not presented for brevity.

5 Application of the optimized model: out-of-plane response of one-way spanning URM walls subjected to relative support motion

The simplified numerical model showed good accuracy and efficiency in reproducing the outcomes of the benchmark experiment. It can simulate the detailed one-way bending out-of-plane responses under a single 20-s loading run in 1.3 h (average value depending on the hardware). Although more demanding compared to well-established and simpler approaches [55], such computational time is deemed reasonable for research purposes and considering the higher accuracy the model presents. Moreover, the procedure presented in this study is more versatile and can be employed for simulating more complex behaviors as well as representing the correct texture and typology of the walls. For example, such model represents a powerful tool to investigate the influence of different parameters on the dynamic one-way bending out-of-plane behavior of masonry walls. This allows for extrapolation of the current knowledge and generating new data for the cases that have not been studied due to experimental constraints or the limitations of previous numerical approaches. One attractive application is exploring the role of changing boundary conditions on the out-of-plane response of walls. The motivation behind this can be explained by the fact that walls of real-world buildings may experience more complex scenarios compared to the idealized conditions considered in the experiments. The consequence of the discrepancy between the conceptualized static boundary conditions and those governing the actual dynamic response is a well-known effect in the literature, as already mentioned in the introduction [8, 15–17, 56].

For example, unlike in the benchmark test, in a real building the motion transferred to the top and bottom boundaries of the wall might differ in amplitude and frequency content due to the filtering effect of the global response of the building. The supports of out-of-plane loaded masonry walls in a building are subjected to a motion that is filtered and amplified by the building structure, which, in some cases, can be significantly different from the ground motion. Such motion at the boundaries of the walls is primarily affected by: i) the diaphragm response, notably the in-plane or membrane flexibility of the diaphragms in the building, and ii) the filtering and amplifying effect due to the building structure, particularly the shear walls [57]. Thus, this effect can vary depending on the position of the wall within the structure, the type of floor diaphragms, the intensity of the ground motion, and the amount of global structural damage accumulated from previous loading events during the lifetime of the structure.

The performance of URM walls subjected to out-of-plane support motion accounting for such factors has been the topic of only a few studies so far [15, 16, 58–60]. However, all of these studies unequivocally indicate that URM walls appear to be more vulnerable when they are subjected to relative out-of-plane support motions. While relative support motions can be applied to numerical models with multiple-degrees-of-freedom (MDOF), this approach cannot be adopted for single-degree-of-freedom (SDOF) modeling approaches, which typically apply the bottom motions obtained from real-world events or building experiments [40, 61–63]. Such SDOF systems are typically defined based on the dynamic equivalence of their elastic properties (vibration period and viscous damping) and on their comparability with the nonlinear hysteretic behavior obtained

from MDOF models. When appropriately defined, SDOF models can efficiently interpret the seismic response of MDOF systems with significantly lower computational effort, particularly in cases where the seismic response is dominated by a single mode of deformation. This is especially relevant for one-way bending URM walls in the out-of-plane (OOP) direction, where the response is largely governed by a single deformation mode. As a result, SDOF models remain widely used and particularly attractive for the OOP seismic assessment of individual URM walls due to their minimal computational effort, especially for large-scale seismic risk investigations requiring a substantial number of nonlinear dynamic analyses. While static methods, such as linear or non-linear kinematic analysis, are usually preferred in practice for the OOP assessment of one-way spanning walls, dynamic analysis conducted by means of SDOF and high-fidelity models, such as the one presented in this study, typically results in less conservative outcomes and can provide a more straightforward interpretation of the wall response. For instance, dynamic analysis can clearly identify wall collapse, rather than relying on an arbitrary definition of the dynamic point of instability, often defined as a fraction of the static point of instability.

Thus, the focus of the current study is not only to investigate this effect but also to attempt to find a solution that can be adopted for SDOF models by means of a sensitivity study. The results of this sensitivity study are expected not only to further extend the understanding of the interplay between the dynamic global in-plane behavior of buildings and the local dynamic response of out-of-plane walls, but also to improve methodologies that are widely used in engineering practice. The next subsections explain the conducted sensitivity study in more detail.

5.1 Definition of motions at wall boundaries

The signals used for loading the numerical specimen under the different top and bottom motions are collected from the shake-table test conducted by Graziotti et al. [64] on a two-story cavity wall building (referred to as EUCENTRE-1 building). This allows selecting motions representative of the expected conditions in actual structures. As shown in Fig. 11a, the structure is a cavity specimen with an inner calcium silicate leaf and outer clay leaf, tested under 24 consecutive unidirectional earthquake loading representative of induced seismicity in the Groningen area in the period the study was carried out. Additionally, model identification white noise runs were conducted, as reported in Table 4. The specimen is found appealing to the current study for several reasons. To begin with, the inner leaf is constructed with materials similar to the one-way bending benchmark simulated by the numerical model. Besides, the spacing between

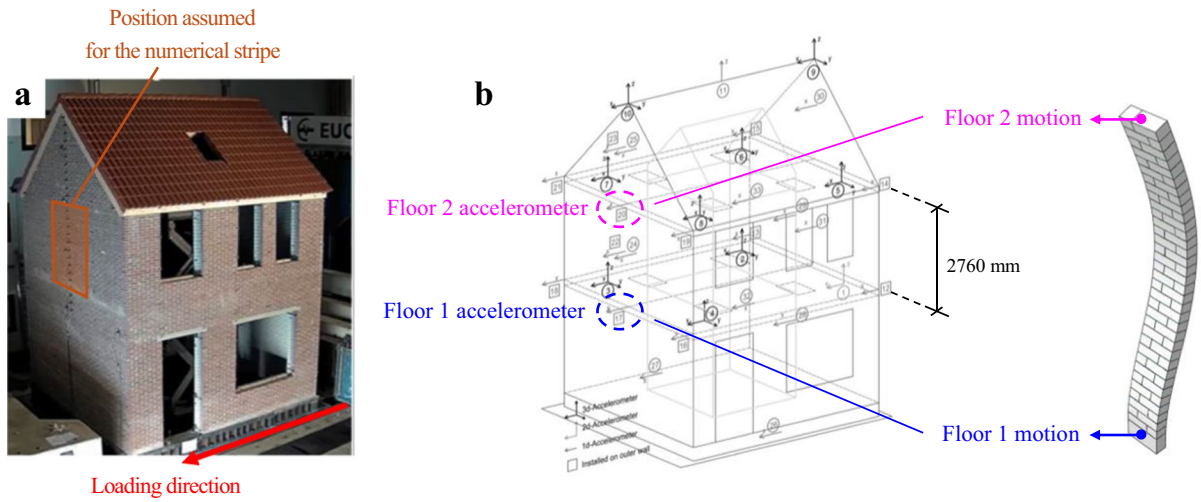

Fig. 11 Visual description of the methodology for simulating the effect of dynamic boundary conditions: view of the reference building [65] (**a**) and location of the sensor for obtaining the differential top and bottom motions (**b**)

Table 4 Loading runs used for the testing of the EUCENTRE-1 building [64]

Run #	Input	Scale	PTA* [g]	Run #	Input	Scale	PTA [g]	Run #	Input	Scale	PTA* [g]
1	WN	–	–	9	EQ1	150%	0.137	17	WN	–	–
2	EQ1	25%	0.024	10	WN	–	–	18	EQ2	50%	0.114
3	WN	–	–	11	EQ2	30%	0.064	19	EQ2	125%	0.194
4	EQ1	50%	0.050	12	EQ2	30%	0.059	20	WN	–	–
5	WN	–	–	13	EQ2	30%	0.056	21	EQ2	150%	0.243
6	EQ1	50%	0.050	14	EQ2	50%	0.087	22	WN	–	–
7	EQ1	100%	0.099	15	WN	–	–	23	EQ2	200%	0.307
8	WN	–	–	16	EQ2	100%	0.170	24	WN	–	–

*Recorded peak table acceleration

the floors of the building specimen is 2760 mm, similar to the height of the numerical wall specimen. It is assumed that the 1.5-brick model represents a stripe of the wall perpendicular to the loading direction and is located on the second story of the experimental building, where more difference is expected in the motion of the boundaries. Hence, the acceleration data recorded from the second and first floors of the building are used to excite the top and bottom of the numerical stripe, as shown in Fig. 11b.

Instead of using the data of all loading runs, only the runs during which the building's behavior changed due to the appearance and evolution of damage are considered. Specifically, four different damage levels are identified in the behavior of the building based on visual inspection of crack propagations. As indicated in the crack propagation maps of the building in Fig. 12, the damage levels include a no-damage condition (DL1), light damage (DL2), moderate damage (DL3), and a near-collapse condition (DL4). While the motions of the first and second floors are quite similar in DL1 due to the presence of rigid slabs, they become increasingly different as damage progresses. This damage manifests as widening diagonal shear and in-plane flexural cracks, damage to masonry spandrels, and horizontal cracks at the connections between the walls and the base of the roof. By DL4, the longitudinal walls were observed to have reached their full in-plane force capacity, with slender piers exhibiting flexural rocking behavior. These factors collectively resulted in progressively different motions between the first and second floors as the damage states advanced. Hence, only the acceleration data collected from the loading runs corresponding to the observation of each of the aforementioned damage states were used for the simulations. These include runs 11 (DS1), 16 (DS2), 19 and 21 (DS3), and 23 (DS4), as highlighted in Table 4. Both runs 19 and 21 are presumed to represent two different states of the moderate damage condition (DS3) since both show new cracks but remain in the same category of damage.

The high-intensity portions of the first- and second-floor signals extracted from the five loading runs mentioned above, the average value of those signals, and their spectral acceleration content and displacement time histories are shown in Fig. 13. The first-floor signal is scaled to a PGA of 1 g in each graph, and the second-floor data is scaled proportionally. All signals are cleaned via a fourth-order Butterworth bandpass filtering between the 0.1 to 50 Hz frequency. The graphs show a considerable change in the spectral content of both floor accelerations when moving from no damage to light damage. Moreover, a gradual shift of the peaks of both floors (indicated with vertical lines in the figures) towards higher periods is observed with the progression of the damage level. Interestingly, although the shapes of the spectrums of both floors remain similar until run 21, they show more difference at the last damage state, implying a change in the phase of the motions at the near-collapse conditions. The vertical black lines in the graphs indicate the first-mode frequency of the numerical stripe.

Two simplifications are made in the loading procedure. Firstly, while the input motions are obtained from a building under incremental damages maintained from a consecutive loading sequence, they are applied to a pristine numerical specimen. In other words, the numerical simulations do not reflect the cracking and damage of the out-of-plane wall in the reference building at certain damage states. This was done to maintain the focus on the changes in the response of the pristine wall subject to increasingly

Fig. 12 Damage levels of the EUCENTRE-1 building identified based on its crack propagations [65]

different motions rather than on the damage accumulation. Secondly, in contrast with the previous sections, where the numerical specimens were analyzed under a consecutive loading sequence, the accelerations collected from each run of the building experiment are applied separately during single-run simulations. In this manner, each signal is scaled up to different intensities (with 0.2 g increments) until collapse under different acceleration profiles is reached.

Three types of simulations are conducted for the acceleration profiles collected from each damage state: one by applying the differential motions to the boundaries, one by using the first-floor motion at both boundaries, and one by imposing the average of the two floor motions to both boundaries. The second loading scenario is used to compare the behavior of the specimen with and without considering the effect of differential motions and to explore the importance of the amplification of motion transferred to the different floors. The third scenario is considered to investigate the possibility of a simple solution that can be adopted for SDOF models, where the application of different motions at the top and bottom is not feasible due to the presence of just a single degree of freedom.

It should be noted that the approach of selecting input motions from a building experiment is adopted neither for a subsequent comparison of the response of the 1.5-stripe model against that of the wall in the building specimen, nor assuming that the 1.5-stripe represents the wall of the building. In other words, the study of this section is not intended for the prediction of the behavior of the two-way-spanning wall in the building specimen. In fact, it should be clarified that the motions extracted from the building experiments are only meant to facilitate the sensitivity study through supplying the authors a set of differential motions that are consistent with real-world recording instead of arbitrarily choosing boundary motions simply based on educated guess.

5.2 Numerical results

The results of analyzing the 1.5-brick stripe under the three loading scenarios and five acceleration profiles (with 0.1 MPa vertical pre-compression) are illustrated in Fig. 14. The acceleration profiles are identified by the level of damage state and the loading run they are obtained from the building experiment. For example, the DS2-16 profile belongs to the signals of the loading run 16 for EUCENTRE-1 building, which has been identified as the onset of the second damage state in the response of the building. Figure 14a includes the maximum peak ground acceleration (PGA) experienced by the specimen up to its collapse under each acceleration profile. In the case of the application of differential loading, the specimen shows a general decrease in the collapse PGA when subjected to loading profiles of higher damage states, failing at a 17% lower PGA under the DS3-21 profile than when subjected to the loadings from the non-damaged building (DS1-11). This suggests the importance of considering the structural amplification effects in the dynamic analyses of URM walls subjected to out-of-plane loading. The analyses under the DS2-16 profile show an outlier response for the case of the application of differential motions, since the relative motion of the boundaries improves the out-of-plane performance, and the collapse PGA increases by 8%. This unexpected condition occurs because a complete failure mechanism of the wall activates but the simultaneous movement of the top boundary in the opposite direction drags the wall back to a stable condition. As a result, collapse is achieved only in the following loading increment. The transition to the last loading profile (DS4-23) shows another exception for all the conducted simulations. For this loading profile, the collapse PGA increases compared to the DS3-21 loading scenario, which may be caused by the changes in the frequency content of the motions. As shown in Fig. 13, the DS3-21 s-floor signal shows a higher spectral acceleration at the frequency of the numerical wall compared to the DS4-23 signal. This special occurrence highlights the difficulty of deriving conclusions from a single set of analyses under dynamic conditions. It is therefore important to highlight that the results presented in this section showcase the potential of the calibrated model and provide some preliminary insight on the topic. However, they are far from being exhaustive for investigating the out-of-plane response of one-way spanning URM walls subjected to relative support motion, which requires the analysis of a larger number of wall configurations and applied motions.

Figure 14(b) illustrates the variation in the collapse PGA under each acceleration profile when the specimen is subjected to either the average of floor motions or the first-floor motion equally applied to its top and

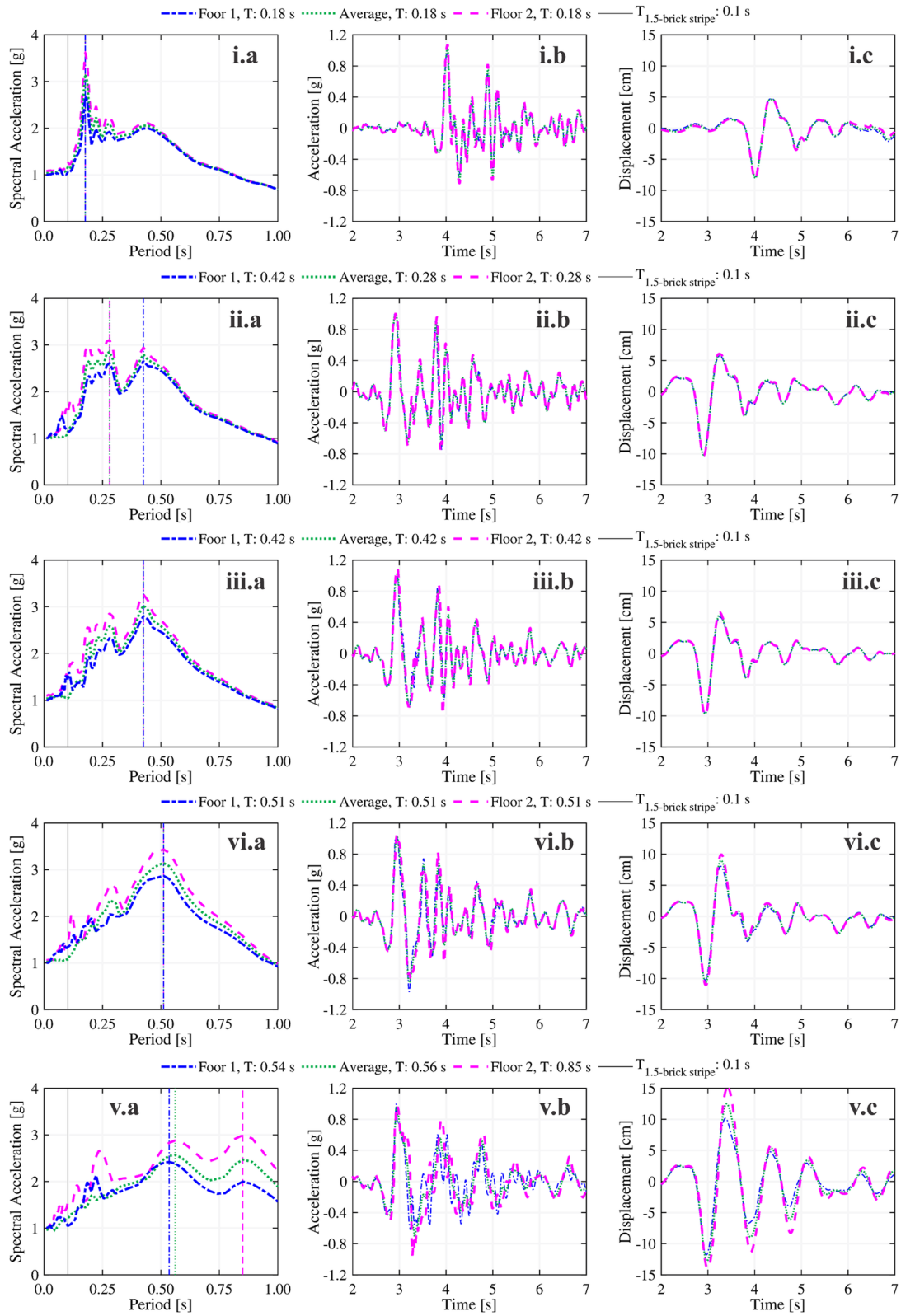
Foor 1, T: 0.18 s
Average, T: 0.18 s
Floor 2, T: 0.18 s
T1.5-brick stripe: 0.1 s
i.a
i.b
i.c
Foor 1, T: 0.42 s
Average, T: 0.28 s
Floor 2, T: 0.28 s
T1.5-brick stripe: 0.1 s
ii.a
ii.b
ii.c
Foor 1, T: 0.42 s
Average, T: 0.42 s
Floor 2, T: 0.42 s
T1.5-brick stripe: 0.1 s
iii.a
iii.b
iii.c
Foor 1, T: 0.51 s
Average, T: 0.51 s
Floor 2, T: 0.51 s
T1.5-brick stripe: 0.1 s
vi.a
vi.b
vi.c
Foor 1, T: 0.54 s
Average, T: 0.56 s
Floor 2, T: 0.85 s
T1.5-brick stripe: 0.1 s
v.a
v.b
v.c
Spectral Acceleration [g]
Period [s]
Acceleration [g]
Displacement [cm]
Time [s]

◂**Fig. 13** Overview of the floor motions extracted from the EUCENTRE-1 building: 5%-damped spectral acceleration (**a**), acceleration time-history (**b**), and displacement time-history (**c**) for DS1-11 (i), DS2-16 (ii), DS3-19 (iii), DS3-21 (iv), and DS4-23 (v) loading profiles

bottom, normalized with respect to the collapse PGA obtained for the application of the original differential motions at the wall boundaries. The graph shows that the application of the first-floor motion tends to overestimate the collapse PGA. An exception is again represented by the DS2-16 profile, for which the unexpected over-resistance experienced by the wall during the application of differential motions has already been discussed. The application of averaged accelerations overall provides a closer estimation of the collapse PGA during the simulations with the lower-damage loading profiles, once again with the exception of the DS2-16 profile. In contrast, the application of averaged accelerations leads to the same 8% and 16% overprediction of the collapse PGA observed during the application of the base acceleration under higher-damage DS3-21 and DS4-23 profiles, respectively. This may be caused by the increased difference in amplitude and phase of the motions at the boundaries of the wall. This generates larger relative displacements between the top and bottom wall supports and undermines the development of the vertical arching effect that occurs due to the opening of the flexural cracks. Such a reduction of the wall confinement leads to lower PGA collapse values. However, this effect is completely overlooked when identical motions are applied to both boundaries, leading as a consequence to an overprediction of the wall capacity.

6 Conclusions

This paper presents a numerical procedure to simulate the dynamic response of out-of-plane masonry walls. The procedure is then applied to simulate the mechanical response of a one-way spanning calcium-silicate masonry wall subject to incremental dynamic testing. A state-of-the-art damaging block-based modeling strategy has been employed to model the masonry. Such a model has been here used for the first time in a dynamic regime, utilizing an HHT time integration scheme and Rayleigh damping in the bulk (expanded blocks), capturing the dynamic response under incrementally increasing earthquake loading up to structural collapse. The main findings of the paper can be summarized as follows:

- A comprehensive modeling procedure was laid out, including constructing the geometry, calibrating material constitutive behaviors, applying proper boundary and loading conditions, and setting up the solvers.
- The implementation of Rayleigh damping in the expanded blocks of the numerical model regularizes the response under dynamic loads and allows simulating the energy dissipation observed in real-world structures. The use of the implicit solver allows the complete utilization of the Rayleigh damping without the limitations of explicit solvers.
- For the case under study, the adoption of a 5% damping ratio yields a good prediction of the experimental response in terms of force–displacement hysteresis, as well as acceleration and deformation time histories.
- After validating the modeling procedure against the experimental benchmark, the computational efforts of the numerical simulation that reproduces the entire wall in one-way bending are reduced by 76% by replacing the complete geometry with a representative 1.5-brick stripe. Such simplification does not affect the accuracy of the prediction. Removing low-amplitude runs that do not influence the response of the model further enhanced the analysis time by 13%.
- The optimized numerical model is adopted to investigate the effect of differential top and bottom motion on the one-way bending dynamic behavior of masonry walls. The results of such a study highlight the importance of simulating the relative motion. Alternatively, using the average of the motions for both the top and both boundaries represents a valid alternative in the case of limited damage to the building where the wall is located, and therefore, the difference between the motions is limited.

The simulation methodology presented in this study allows for modeling complex dynamic behaviors that have not been explored previously. The study of the differential boundary motions presented in this paper can be extended to variations of walls having

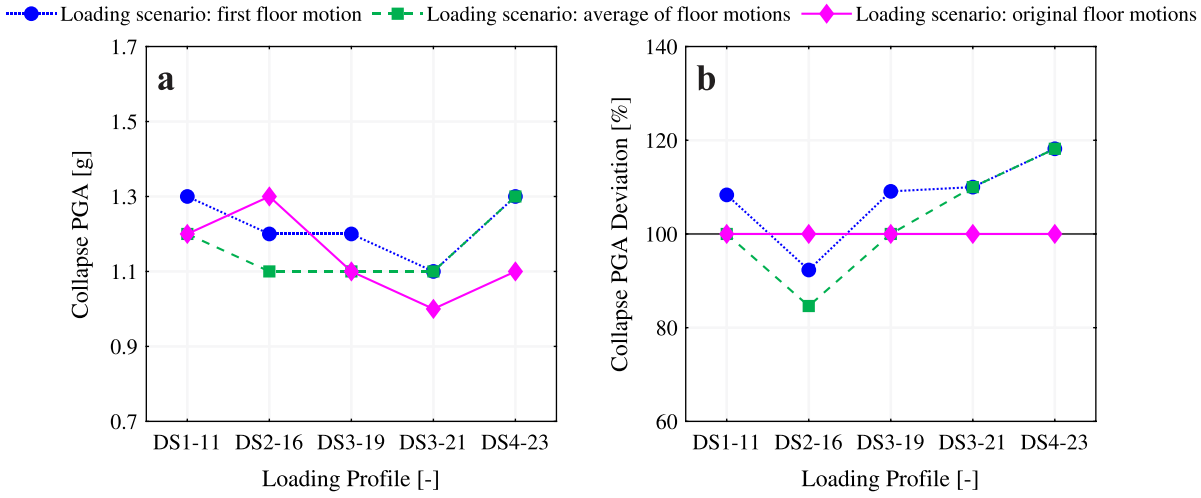

Fig. 14 Performance of the simplified numerical specimen under differential top and bottom motions: effect of loading acceleration profiles (**a**) and effect of loading scenario (**b**)

different slenderness ratios, material properties, pre-compression levels, and top constraints. Doing so would allow the identification of the most important parameters influencing the extent of the effect of dynamic boundary conditions, and confirm the validity of the preliminary results described in this paper. Moreover, the same study can be carried out for the acceleration data obtained from buildings with flexible floor diaphragms [20]. Additionally, the influence of ground motion can be investigated by using the response of structures under tectonic earthquake loading [45]. Finally, along with continuing the sensitivity study on dynamic boundary conditions for the one-way bending wall simulated herein, the modeling procedure can be employed to reproduce the more complex response of the two-way bending return walls with different boundary conditions and geometries [46, 47]. Such investigations could help to refine the less detailed modeling strategies and advance the understanding of the dynamic structural behaviors of masonry walls.

Acknowledgements All experimental data used as a benchmark in this paper was produced as part of the "Study of the Vulnerability of Masonry Buildings in Groningen" project at the EUCENTRE Foundation, Pavia, Italy. This project was undertaken within the framework of the research program for hazard and risk of induced seismicity in Groningen, sponsored by the Nederlandse Aardolie Maatschappij BV. The authors thank the EUCENTRE Foundation for providing ready access to the data.

Author contribution AG: Conceptualization, Methodology, Software, Validation, Formal analysis, Investigation, Data Curation, Resources, Writing – Original Draft, Writing – Review and Editing, Visualization, Funding acquisition. AMD: Methodology, Validation, Writing – Original Draft, Writing – Review and Editing, Supervision, Funding acquisition. SS: Conceptualization, Methodology, Validation, Data Curation, Writing – Original Draft, Writing—Review & Editing, Supervision. PBL: Validation, Writing – Review & Editing, Supervision, Funding acquisition. JGR: Conceptualization, Validation, Writing – Review & Editing, Supervision, Project administration, Funding acquisition. FM: Conceptualization, Methodology, Validation, Resources, Data Curation, Writing—Original Draft, Writing – Review & Editing, Supervision, Project administration, Funding acquisition.

Funding This project was supported by the Erasmus + programme of the European Union under the Staff Mobility Grant for Training. This project has also received funding from the European Union's Horizon 2020 research and innovation programme under the Marie Sklodowska-Curie grant agreement No 101029792. This study has been also funded by the STAND4HERITAGE project (new STANDards FOR seismic assessment of built cultural HERITAGE) that has received funding from the European Research Council (ERC) under the European Union's Horizon 2020 research and innovation program (Grant No 833123) as an Advanced Grant.

Data availability No datasets were generated or analysed during the current study.

Declarations

Conflict of interest The authors declare no competing interests.

Appendix: Detailed description of the numerical modeling approach

Further details about the numerical modeling approach adopted in this study are presented herein.

Appendix 1: Geometry and discretization

An overview of the block-based modeling approach developed in [18] is shown in Fig. 15. The contact algorithm which rules the interaction between blocks adopts the penalty method [19] and a master–slave formulation [66]. In summary, the contact is established at discrete points on the slave surface, where each slave node of the slave surface (green nodes in the figure) is related to multiple points on the master surface (red surfaces in the figure). These so-called node-to-surface interactions are based on the external nodes of the meshed expanded blocks. The response of the joints is governed by the relative displacement of slave nodes with respect to the master surface in normal and tangential directions. Here, finite sliding formulation is used for the calculation of separation, sliding, and rotation of the surfaces [20]. The use of discrete node-against-surface contact definitions is preferred over adopting cohesive [22, 26] or interface elements [21, 25] for several reasons. Firstly, contact algorithms better handle larger displacements without technical issues such as element distortion. Secondly, they do not require a conforming or geometrically-compatible meshing of the contacting surface pairs. Finally, since they are not assigned with geometrical representation and hence do not have mass, their large stiffness does not directly influence the stable time-stepping increment size of the implicit solver used in this study.

Each expanded block is discretized into a 4×2×2 (length×height×thickness) array of hexahedral finite elements with first-order interpolation for the

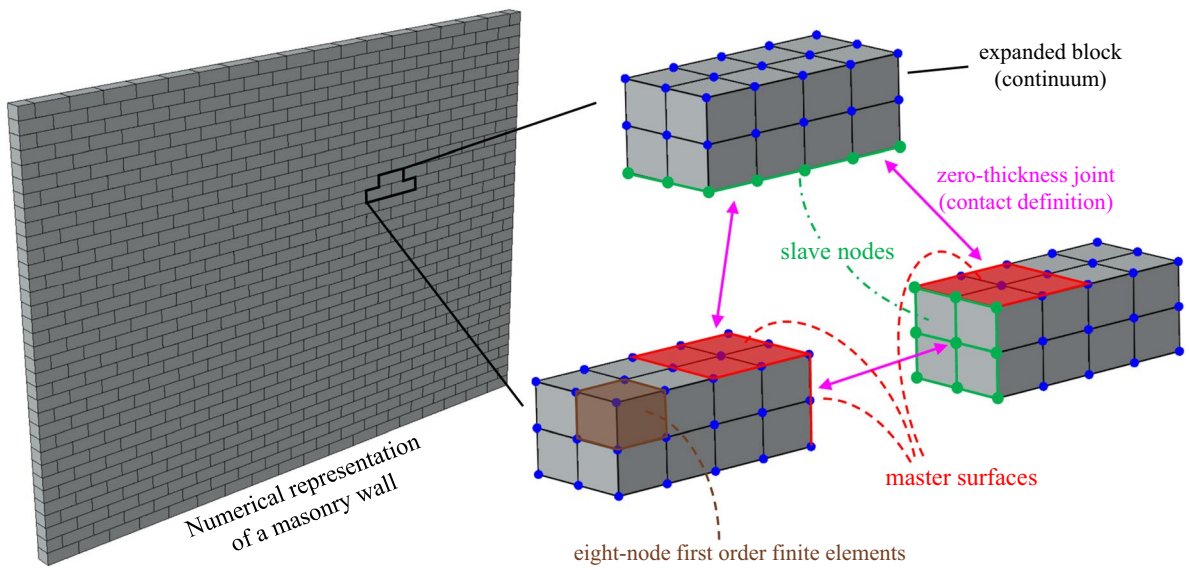

Fig. 15 Overview of the block-based modeling approach developed in [18]

displacement fields [67]. Such discretization presents the coarsest mesh to be used for the study of wall-level behaviors and is achieved over extensive sensitivity studies during the simulation of in- and out-of-plane quasi-static cyclic wall experiments [33]. The two elements accommodated in the height are required for the proper distribution of compressive stresses. The four longitudinal elements are needed to avoid shear-locking of the expanded blocks during in-plane deformations. The two thickness elements are needed for capturing flexure during out-of-plane motions. Moreover, such discretization is required to avoid ill-defined interactions for the zero-thickness joints, as the contacts are enforced at the exterior nodes of the expanded blocks. The three and five contact points in the height and length directions are sufficient for the correct definition of the vertical and horizontal mortar joints, respectively. The three contact points along the thickness are the minimum required for capturing the out-of-plane response with sufficient accuracy. Any finer discretization is shown to increase unreasonably the computational effort associated with wall-level simulations without noticeable effect on the accuracy or the outcomes [33]. In instances with complex geometries or large number of active expanded blocks, the use of finer mesh may also result in the abortion of the analysis due to the high number of active contact definitions [20].

Appendix 2: Joint nonlinear behavior

The detailed non-dilatant nonlinear response of zero-thickness joints is shown in Fig. 16. The maximum allowable contact tensile (σ_t) and shear (τ) stresses in a contact point, respectively, are defined after failure as:

$$\sigma_t = (1 - D)f_t, \tau = (1 - D)c + \langle -\sigma \rangle \tan\phi \quad (1)$$

being f_t the tensile strength, c the shear cohesion, ϕ the friction angle, σ the current normal stress (shown with green color in Fig. 16), and $0 \le D \le 1$ the joint degradation scalar variable. The latter is here assumed to linearly vary along with the joint opening/slip, and to couple tensile and shear cohesive responses, as expressed as:

$$D = \max\left(\frac{u^+_{max} - f_t/k_{nt}}{u_k}, \frac{|\delta_{max}| - c/k_s}{\delta_k}\right) \quad (2)$$

where k_{nt} is the normal stiffness of the joint in tension, k_s is the cohesive-shear stiffness of the joint in

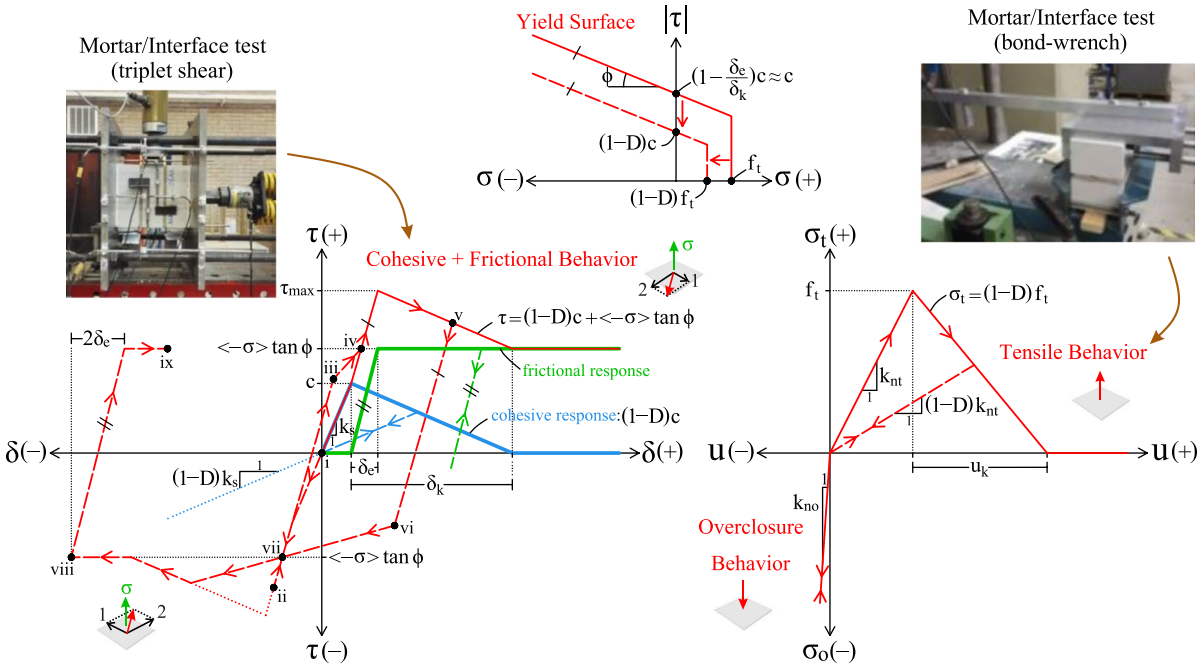

Fig. 16 Shear (left) and normal (right) cyclic behaviors and yield surface (middle) of zero-thickness joints

shear, and u^{+}_{max} and $|\delta_{max}|$ are the maximum normal opening and slip experienced at each contact point, respectively. Accordingly, the degradation of cohesion in shear is coupled with the degradation in tension, and vice versa. Finally, u_k and δ_k represent the maximum allowed opening and slip, respectively, from the maximum of cohesion (D = 0) to the total degradation of the contact point (D = 1). For simplicity, u_k and δ_k are here assumed to be equal in magnitude. The "+" superscript used in the first term of Eq. 2 indicates that the overclosure of the contact does not increase the degradation scalar, whereas the |x| absolute function is used in the second term to take into account the evolution with respect to the slip direction. The $\langle x\rangle = (|x| + x)/2$ Macaulay bracket function shows that the frictional response is only obtained under compressive normal stresses. The frictional response, characterized by a constant elastic slip (δ_e) is here supposed to be activated, for simplicity, at the start of cohesive degradation (i.e., upon attaining peak cohesion) and reaches its steady-state value ($\langle-\sigma\rangle\tan\phi$) after a slip equal to δ_e. In this way, the initial linear elastic shear joint response is fully characterized by the cohesive-shear stiffness k_s. It should be pointed out that due to the slight delay in full attainment of the frictional resistance, the peak shear strength is slightly lower than the arithmetic summation of cohesion and friction, i.e., $\tau_{max} = \left(1 - \delta_e/\delta_k\right)c + \langle-\sigma\rangle\tan\phi$ given that $\delta_e \ll \delta_k$.

In cyclic regime, the reduced stiffness used for the tensile- and shear-cohesive behaviors is calculated with a reduction equal to the degradation sscalar variable (D) and unloading to the origin. On the contrary, the shear-frictional response of the joints adopts an elastic loading–unloading-reloading stiffness via the constant elastic slip concept. Hence, the overall cyclic shear response follows the sum of both the cohesive and frictional contributions. Finally, since elasticity modulus of masonry wallet (E_m) is adopted for the expanded blocks, linear elastic behavior with high loading–unloading stiffness (k_{no}) is adopted for the joints under compressive forces, resulting in negligible penetrations. Based on the abovementioned information, example of sequences for the cyclic behaviors of the joints are shown in Fig. 16. Specifically for the shear response, the sequence starts from the origin (point i), reaching a post elastic state where cohesive damage has initiated and friction is being developed (point ii). Then the direction of the loading is changed and increased until complete frictional response is attained and the cohesive response is further degraded (point v). Afterwards, the loading direction is changed again and the joint is loaded until complete loss of cohesive response, showing a purely frictional behavior (point viii). The loading direction is reversed for one last time and the constant frictional resistance is achieved once more (point ix). Specifically for the unloading stiffness during the first change in the loading direction (from point ii to v), the cyclic behavior first follows up to point iii the same stiffness value used during the elastic slip phase, followed by reduced stiffness. The vertical distance between points ii and iii is equal to twice the frictional resistance developed up to point ii. A similar behavior is observed during the second change in loading direction (between points v and viii). In this case the complete frictional resistance has already been developed, so that the vertical distance between the load reversal point (v) and the stiffness change point (vi) is equal to $2\langle-\sigma\rangle\tan\phi$. It should be noted that both focal points iv and vii at which the cyclic behavior under reverse-loading intersects with the envelop of the shear response are pre-determined and fixed at the peak of the shear-frictional resistance, i.e. $\langle-\sigma\rangle\tan\phi$.

Appendix 3: Expanded block nonlinear behavior

Concerning the nonlinear response of expanded blocks, Fig. 17 shows the uniaxial tensile and compressive behaviors based upon two independent scalar damage variables for compressive ($0 \le d_c < 1$) and tensile ($0 \le d_t < 1$) responses as:

$$\sigma^{-} = \left(1 - d_c\right)E_m\left(\varepsilon^{-} - \varepsilon^{-}_{p}\right), \sigma^{+} = \left(1 - d_t\right)E_m\left(\varepsilon^{+} - \varepsilon^{+}_{p}\right) \tag{3}$$

where E_m is the initial Young's modulus of the expanded blocks, σ^- and σ^+ are the maximum allowable compressive and tensile uniaxial stresses, ε^- and ε^+ the compressive and tensile uniaxial strains, and ε^-_p and ε^+_p are the relative plastic strains. Based on the simplified behaviors adopted explained in Sect. 2.1, it is herein assumed that compressive damage initiates at the end of the plateau ($d_c = 0$) and increases proportional to the loss of compressive strength, reaching $d_c = 0.9$ by the end of the softening regime.

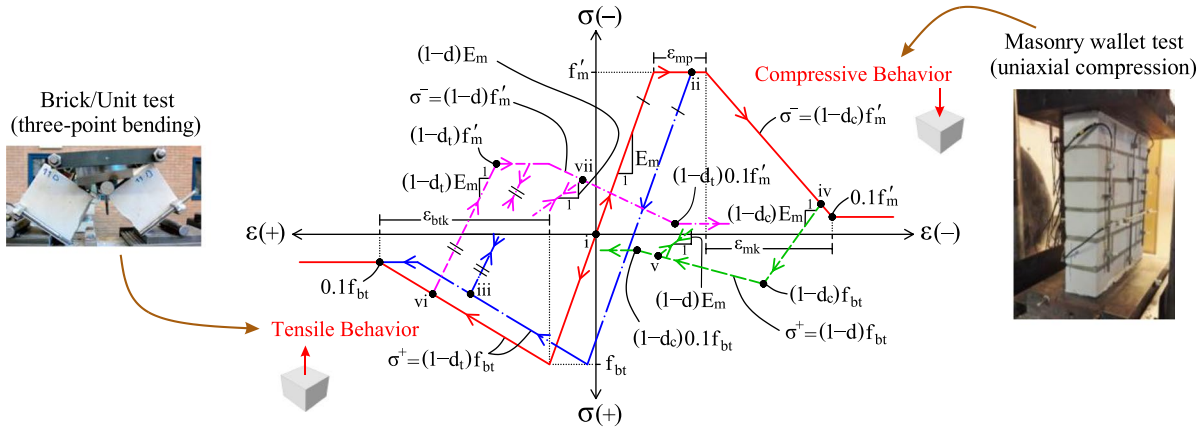

Fig. 17 Expanded blocks uniaxial compressive-tensile response

Similarly, the onset ($d_t = 0$) and end ($d_t = 0.9$) of the tensile damage evolution is considered to coincide with the start and the end of the tensile softening phase. This assumption can be expressed as:

wherein, f_m' is the uniaxial compressive strength of

$$d_c = \begin{cases} 0 & |\varepsilon^-_{max}| \le {f_m'}/{E_m} + \varepsilon_{mp} \\ 0.9\dfrac{|\varepsilon^-_{max}| - \left({f_m'}/{E_m} + \varepsilon_{mp}\right)}{\varepsilon_{mk}} & {f_m'}/{E_m} + \varepsilon_{mp} < |\varepsilon^-_{max}| \le {f_m'}/{E_m} + \varepsilon_{mp} + \varepsilon_{mk} \\ 0.9 & |\varepsilon^-_{max}| > {f_m'}/{E_m} + \varepsilon_{mp} + \varepsilon_{mk} \end{cases}$$

$$d_t = \begin{cases} 0 & \varepsilon^+_{max} \le {f_{bt}}/{E_m} \\ 0.9\dfrac{\varepsilon^+_{max} - {f_{bt}}/{E_m}}{\varepsilon_{btk}} & {f_{bt}}/{E_m} < \varepsilon^+_{max} \le {f_{bt}}/{E_m} + \varepsilon_{btk} \\ 0.9 & \varepsilon^+_{max} > {f_{bt}}/{E_m} + \varepsilon_{btk} \end{cases} \quad (4)$$

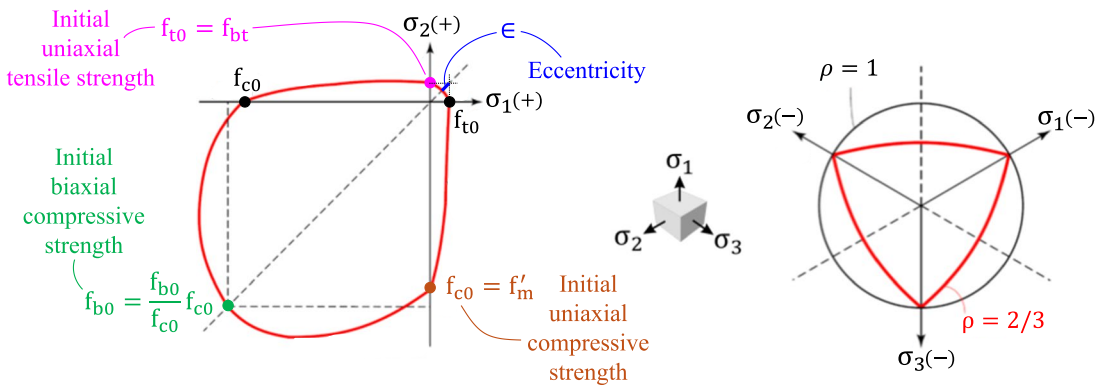

Fig. 18 Expanded blocks yield surface in plain strain (left) and deviatoric plane (right)

masonry wallets, f_{bt} is the direct tensile strength of masonry units, and ε^{-}_{max} and ε^{+}_{max} are the maximum uniaxial compressive and tensile strains ever experienced at the integration point within the finite element during its loading history, respectively. Hence, the compressive and tensile plastic strains will be equal to zero in the elastic phases and equal to $\varepsilon^{-} - f_m\prime/E_m$ and $\varepsilon^{+} - f_{bt}/E_m$. , respectively, in post-peak regimes. Therefore, the maximum allowable stresses in tension and compression can be expressed as

$$\sigma^{-} = \begin{cases} E_m\varepsilon^{-} & |\varepsilon^{-}| \le f_m\prime/E_m \\ (1-d_c)f_m\prime & \text{elshere} \end{cases}, \sigma^{+} = \begin{cases} E_m\varepsilon^{+} & \varepsilon^{+} \le f_{bt}/E_m \\ (1-d_t)f_{bt} & \text{elsewhere} \end{cases} \tag{5}$$

During compressive softening (point iv, where d_c is non-zero), the entire tensile regime (σ^{+} in Eq. 5 is scaled down by a factor of $(1-d_c)$. The peak and residual tensile strengths are reduced to $(1-d_c)f_t$ and $(1-d_c)0.1f_{bt}$, respectively, and the softening response is determined by the coupled damage scalar (d). Similar behavior is observed in the third instance (dash-dot purple line) for a cyclic response initiated during tensile softening (point vi), where the compressive regime (σ^{-} in Eq. 5 is scaled by $(1-d_t)$.

In the cyclic regime, the damage scalars of Eq. 5 are used for the prescription of stiffness reductions as explained in Sect. 2.1. The compressive and tensile cyclic behaviors are coupled via the coupling damage scalar ($0 \le d < 1$) defined as

$$d = 1 - (1-d_c)(1-d_t) \tag{6}$$

The detailed exemplification of the cyclic behavior is shown in Fig. 17, by means of three different cases, all starting at the origin (point i). The first instance (dash-dot blue line) shows that a reverse loading from point ii only causes irreversible compressive strains in the model and does not affect further the tensile behavior, since no compressive damage is considered in the plateau region. Accordingly, the stiffness of the subsequent unloading–reloading in the tensile regime (point iii) is only affected by the tensile damage (d_t). On the other hand, in the second instance (dash-dot green line), where the reverse loading is initiated during compressive softening (point iv, where d_c is non-zero), the entire tensile regime (σ^{+} in Eq. 5 is scaled down by a factor of $(1-d_c)$. The peak and residual tensile strengths are reduced to $(1-d_c)f_t$ and $(1-d_c)0.1f_{bt}$, respectively, and the softening response is determined by the coupled damage scalar (d). Similar behavior is observed in the third instance (dash-dot purple line) for a cyclic response initiated during tensile softening (point vi), where the compressive regime (σ^{-} in Eq. 5 is scaled by $(1-d_t)$. The coupled damage scalar (d) is also used to calculate the slope of the subsequent reverse-loading in the next tensile or compressive softening phases of both instances (initiated at points v and vii, for green and purple lines, respectively) by combining the current tensile damage with compressive pre-damage and vice versa. It should be noted that during cyclic behaviors, the lengths of the plateau (ε_{mp}) and softening regimes (ε_{mk} and ε_{btk}) remain unchanged and unaffected by the interaction of the tensile and compressive damages.

The simplified representations of the Drucker-Prager multi-yield surface are shown in Fig. 18. The biaxial compressive strength (f_{b0}) is calculated based on the uniaxial one (f_{c0}, equal to the compressive strength of masonry, $f_m\prime$) using the f_{b0}/f_{c0} parameter. The eccentricity ($\in$) is used to smoothen the yield surface in multi-axial tensile regime. The ratio of the second stress invariant in tensile meridian to the

second stress invariant in compressive meridian (ρ) controls the shape of the multi-yield surface in the deviatoric space. Finally, the dilatancy angle (ψ) governs the dilatancy in expanded blocks via the adopted non-associative flow rule. More detailed description of the multi-yield surface Drucker-Prager type multi-yield surface can be found in [18].

Although several other numerical methodologies (e.g., [27, 68, 69] assume all nonlinear behaviors to occur at the zero-thickness joints for a more efficient structural analysis, the choice of the above constitutive behaviors with nonlinear expanded blocks offers alternative advantages. Firstly, having nonlinear blocks allows for a more accurate representation of certain failure mechanisms, such as diagonal cracking, wherein a realistic damage pattern can form more appropriately when the damages propagate through the blocks rather than being redirected to the joints. Secondly, the use of nonlinear expanded blocks allows for better interaction of loading components and distribution of stresses in the structure under complex loading scenarios (such as combined in-plane and out-of-plane loadings). Thirdly, the accuracy of dynamic analyses is highly dependent on the correct reproduction of the distribution of stresses and energy dissipation within the masonry units, which can be achieved by assigning the expanded blocks with appropriate nonlinear behaviors. This is also consistent with the damping strategy adopted in the current study, as explained in Sect. 2.3. Similarly, the choice of damaged-plasticity-based cyclic behaviors is preferred over the pure plasticity- [21, 25] or damage-based [70, 71] formulations adopted in other works because it better captures the hysteretic energy-dissipation at expanded blocks and joints during dynamic responses. All in all, the adopted constitutive behaviors lead to the versatility of the model and its adaptability to a broad range of structures.

Appendix 4: HHT-α method

The HHT-α time integration method is an extension of the Newmark family of time integration algorithms [35] which solve structural dynamics problems via an equation of motion semi-discretized between the end of the previous time increment (time t_n) and the current one (time t_{n+1}) as expressed as:

$$\left[\left(\frac{1}{\beta_N \Delta t^2}\mathbf{M} + \frac{\gamma_N}{\beta_N \Delta t}\mathbf{C}_{n+1}\right) + \mathbf{K}^{\mathbf{T}}_{n+1}\right] \Delta \mathbf{u}^{k+1}_{n+1} = \left\{\mathbf{f}^{e}_{n+1} - \mathbf{f}^{i}_{n+1}\right\} - \mathbf{M}\ddot{\mathbf{u}}_{n+1} - \mathbf{C}\dot{\mathbf{u}}_{n+1} \tag{7}$$

to obtain the unknown nodal displacements ($\mathbf{u}_{n+1}$), velocities ($\dot{\mathbf{u}}_{n+1}$), and accelerations ($\ddot{\mathbf{u}}_{n+1}$) vectors at t_{n+1} based on those known at t_n. In the equation, the structural mass matrix ($\mathbf{M}$), the current vector of external nodal loads ($\mathbf{f}^{e}_{n+1}$) at t_{n+1}, and the size of the time increment ($\Delta t = t_{n+1} - t_n$) are known. Newton–Raphson (NR) linearization method is used to find the unknowns in a series of iterations to accommodate the effects of material and geometrical nonlinearity. In an ongoing iteration $k+1$, the solver reconstructs the structural tangential stiffness ($\mathbf{K}^{\mathbf{T}}_{n+1}$) and damping matrices ($\mathbf{C}_{n+1}$) as well the internal loads vector ($\mathbf{f}^{i}_{n+1}$) based on the nodal displacement vector calculated at the end of the previous iteration ($\mathbf{u}^{k}_{n+1}$). Moreover, the current nodal accelerations and velocities vectors are recalculated as

$$\ddot{\mathbf{u}}_{n+1} = \frac{1}{\beta_N \Delta t^2}\left\{\mathbf{u}^{k}_{n+1} - \mathbf{u}_n\right\} - \frac{1}{\beta_N \Delta t}\dot{\mathbf{u}}_n - \left(\frac{1}{2\beta_N} - 1\right)\ddot{\mathbf{u}}_n,$$

$$\dot{\mathbf{u}}_{n+1} = \frac{\gamma_N}{\beta_N \Delta t}\left\{\mathbf{u}^{k}_{n+1} - \mathbf{u}_n\right\} - \left(\frac{\gamma_N}{\beta_N} - 1\right)\dot{\mathbf{u}}_n - \frac{\Delta t}{2}\left(\frac{\gamma_N}{\beta_N} - 2\right)\ddot{\mathbf{u}}_n \tag{8}$$

where $\mathbf{u}_n$, $\dot{\mathbf{u}}_n$, and $\ddot{\mathbf{u}}_n$ are the nodal displacements, velocities, and accelerations vectors at the end of increment t_n, respectively. Finally, a new nodal incremental displacements vector ($\Delta \mathbf{u}^{k+1}_{n+1}$) is calculated from Eq. 7 (with appropriate decomposition methods) and the total nodal displacements vector is updated as $\mathbf{u}^{k+1}_{n+1} = \mathbf{u}^{k}_{n+1} + \Delta \mathbf{u}^{k+1}_{n+1}$. The Newmark family of algorithms assume zero initial displacements, velocities, and accelerations when starting the analysis with no previous loading steps ($t = 0$). Alternatively, in the existence of preceding static loading steps, similar to gravity and vertical loading steps in this study, the final displacements of the static steps and zero velocities and accelerations are assumed as the initial conditions for the solver. The solution in each time increment is controlled by the maximum allowed number of NR iterations and the tolerated error in the calculated nodal displacements or internal forces, or other criteria. It should be noted that the error of the solution at time step t_{n+1} is calculated based on the half-step residuals (at $t_n + {}^{\Delta t}/_{2}$) based on the assumption

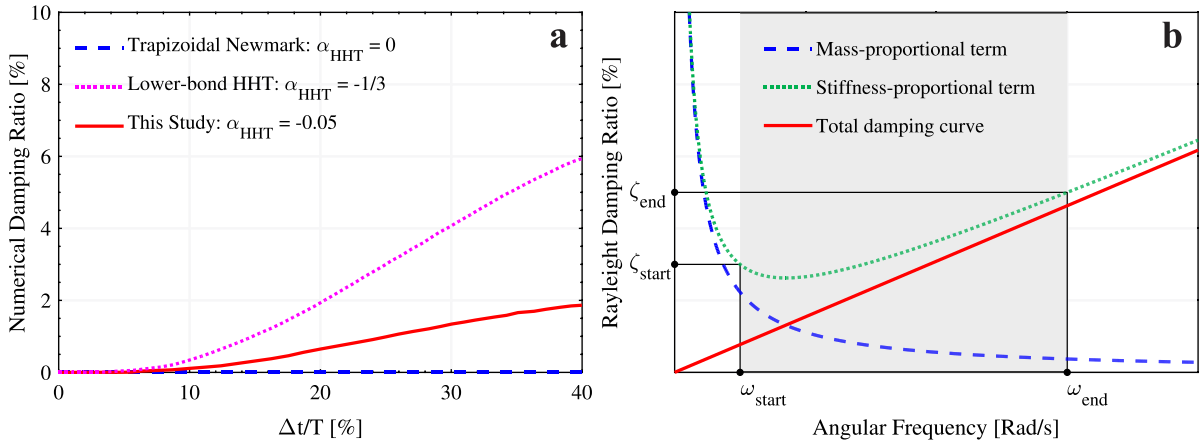

Fig. 19 Overview of damping strategy adopted for dynamic simulations: numerical damping through the HHT implicit solver (**a**) Rayleigh damping implemented in the blocks (**b**)

that the accelerations vary linearly over the time increment [72].

The β_N and γ_N are the parameters conventional to the Newmark family of integrators and can control the numerical energy dissipation. The original Newmark-β integrator adopts a trapezoidal rule (or constant average method) where $\beta_N = 0.25$ and $\gamma_N = 0.5$ and no numerical damping is introduced. Although the solver being unconditionally stable, it fails to maintain second-order accuracy in low-frequency modes as well as control the high-frequency noises. Being a generalized-α method, the HHT method tackles these limitations by introducing numerical damping in the solution through the additional α_{HHT} parameter. Accordingly, Eq. 7 is rewritten as Eq. 9, wherein $\mathbf{f}_n^e$ and $\mathbf{f}_n^i$ are the known vectors of nodal external and internal loads at the end of the previous time increment t_n. The Newmark parameters are also related to α_{HHT} via Eq. 10.

$$\left[\left(\frac{1}{\beta_N \Delta t^2}\mathbf{M} + \frac{(1+\alpha_{HHT})\gamma_N}{\beta_N \Delta t}\mathbf{C}\right) + (1+\alpha_{HHT})\mathbf{K}_{n+1}^{T}\right]\Delta \mathbf{u}_{n+1}^{k+1} = (1+\alpha_{HHT})\left\{\mathbf{f}_{n+1}^e - \mathbf{f}_{n+1}^i\right\} - \alpha_{HHT}\left\{\mathbf{f}_n^e - \mathbf{f}_n^i\right\} - \mathbf{M}\ddot{\mathbf{u}}_{n+1} - \mathbf{C}\dot{\mathbf{u}}_{n+1} \tag{9}$$

$$\beta_N = \frac{1}{4}(1-\alpha_{HHT})^2, \gamma_N = \frac{1}{2} - \alpha_{HHT} \tag{10}$$

In the case of a linear elastic dynamic system, the amount of numerical damping of the response over different periods (T) can be controlled by the parameter $-0.33 \leq \alpha_{HHT} \leq 0$ and the time-stepping increment size (Δt), as shown in Fig. 19a. If α_{HHT} is assumed zero, the algorithm reverts back to the original Newmark-β method with no numerical damping ($\gamma_N = 0.5$) shown with the dashed blue line. On the other hand, $\alpha_{HHT} = -0.5$ provides the maximum artificial damping available from the HHT operator (6% when Δt is 40% of the period of the mode being studied).

The adaptive time incrementation scheme used by the dynamic solver is formulated in [72]. In the case of NR failing to converge within the allowed number of iterations in any time-stepping increment, the solver automatically decreases Δt and re-runs the calculations for a closer target time instance (a new t_{n+1}). The re-incrementation continues until the NR iterations converge and the analysis proceeds to the next increment. If the minimum allowed increment size or the maximum number of allowed re-incrementations are reached and NR does not yield a solution, the analysis halts. In the case of fast convergence in previous time increments, the solver automatically

increases Δt of the subsequent increments (up to a maximum allowed Δt_{max}) for a faster progression of the analysis.

Appendix 5: Rayliegh damping

Through Rayleigh damping, the structural damping matrix ($\mathbf{C}_{n+1}$) at the current time-step (t_{n+1}) can be expressed via one term related to the mass matrix and another term proportional to the current tangential stiffness matrix as in Eq. 11. The damping effects are considered over a range of frequencies starting at starting at f_{start} and ending at f_{end}, and the response in the rest of the frequency domain is overdamped, as shown in Fig. 19b. Hence, the α_R and β_R, which are the Rayleigh mass- and stiffness-proportional damping coefficients are by assigning specific damping ratios to the start and end frequencies (ζ_{start} and ζ_{end}) and solving the linear system of equations shown in Eq. 12. In the equation, angular frequencies ($\omega_{start} = 2\pi f_{start}$ and $\omega_{end} = 2\pi f_{end}$) and dimensionless damping ratios (normalized to 100%) are used for the calculation of Rayleigh coefficients, and target damping ratios are assumed equal for the sake of simplicity ($\zeta_{start} = \zeta_{end} = \zeta_R$). The target frequency range is objective to the natural deformation modes of the structure under study, meaning that f_{start} and f_{end} should be selected based on the modal analysis of the numerical specimen and the frequencies of the desired natural vibration modes as done in Sect. 3.2. It should be noted that the calibration adopted here is for the case of a linear elastic system. In a structure with nonlinear behavior, the amount of damping can be different from the expected one due to the changes in the stiffness of the structure. The consequences of this effect and the approach to tackle such limitation is discussed in Sect. 2.3.

$$\mathbf{C}_{n+1} = \alpha_R \mathbf{M} + \beta_R \mathbf{K}^{\mathbf{T}}_{n+1} \tag{11}$$

$$\begin{cases} \frac{\zeta_{start}[\%]}{100\%} = \frac{1}{2}\left(\frac{\alpha_R}{\omega_{start}} + \beta_R \omega_{start}\right) \\ \frac{\zeta_{end}[\%]}{100\%} = \frac{1}{2}\left(\frac{s_R}{\omega_{end}} + \beta_R \omega_{end}\right) \end{cases} \tag{12}$$

References

1. Hendry EAW (2001) Masonry walls: materials and construction. Constr Build Mater 15(8):323–330. https://doi.org/10.1016/S0950-0618(01)00019-8
2. Frankie TM, Gencturk B, Elnashai AS (2013) Simulation-based fragility relationships for unreinforced masonry buildings. J Struct Eng 139(3):400–410. https://doi.org/10.1061/(ASCE)ST.1943-541X.0000648
3. Moon L, Dizhur D, Senaldi I, Derakhshan H, Griffith M, Magenes G et al (2014) The demise of the URM building stock in Christchurch during the 2010–2011 Canterbury earthquake sequence. Earthq Spectra 30(1):253–276. https://doi.org/10.1193/022113EQS044M
4. Page AW (1991) The newcastle earthquake - behaviour of masonry structures. Mason Int 5:11–18
5. Penna A, Morandi P, Rota M, Manzini CF, da Porto F, Magenes G (2014) Performance of masonry buildings during the Emilia 2012 earthquake. Bull Earthq Eng 12(5):2255–2273. https://doi.org/10.1007/s10518-013-9496-6
6. Oyarzo-Vera C, Griffith MC (2009) The Mw 6.3 Abruzzo (Italy) earthquake of april 6th: on site observations. Bull N Z Soc Earthq Eng 42(4):302–307
7. D'Ayala DF, Paganoni S (2011) Assessment and analysis of damage in L'Aquila historic city centre after 6th April 2009. Bull Earthq Eng 9(1):81–104. https://doi.org/10.1007/s10518-010-9224-4
8. Sharma S, Tomassetti U, Graziotti F, Magenes G (2021) Simplified methodologies for assessing the out-of-plane two-way bending seismic response of unreinforced brick masonry walls: lessons from recent experimental studies. Structures 33:2839–2854. https://doi.org/10.1016/j.istruc.2021.03.121
9. Griffith MC, Lam NTK, Wilson JL, Doherty K (2004) Experimental investigation of unreinforced brick masonry walls in flexure. J Struct Eng 130(3):423–432. https://doi.org/10.1061/(ASCE)0733-9445(2004)130:3(423)
10. Simsir CC, Aschheim MA, Abrams DP (2004) Out-of-plane dynamic response of unreinforced bearing walls attached to flexible diaphragms. In: Proceedings of 13th world conference on earthquake engineering, Vancouver, British Columbia, Canada
11. Penner O, Elwood KJ (2016) Out-of-plane dynamic stability of unreinforced masonry walls in one-way bending: shake table testing. Earthq Spectra. https://doi.org/10.1193/011415EQS009M
12. Giaretton M, Dizhur D, Ingham JM (2016) Dynamic testing of as-built clay brick unreinforced masonry parapets. Eng Struct 127(November):676–685. https://doi.org/10.1016/j.engstruct.2016.09.016
13. Messali F, Ravenshorst G, Esposito R, Rots JG (2017) Large-scale testing program for the seismic characterization of dutch masonry walls. In: 16th World conference on earthquake, Santiago, Chile
14. Graziotti F, Tomassetti U, Penna A, Magenes G (2016) Out-of-plane shaking table tests on URM single leaf and cavity walls. Eng Struct 125:455–470. https://doi.org/10.1016/j.engstruct.2016.07.011

15. Tondelli M, Beyer K, DeJong M (2016) Influence of boundary conditions on the out-of-plane response of brick masonry walls in buildings with RC slabs. Earthq Eng Struct Dyn 45(8):1337–1356. https://doi.org/10.1002/eqe.2710
16. Penner O, Elwood KJ (2016) Out-of-plane dynamic stability of unreinforced masonry walls in one-way bending: parametric study and assessment guidelines. Earthq Spectra 32(3):1699–1723. https://doi.org/10.1193/011715EQS011M
17. Tomassetti U, Correia AA, Candeias PX, Graziotti F, Campos CA (2019) Two-way bending out-of-plane collapse of a full-scale URM building tested on a shake table. Bull Earthq Eng 17(4):2165–2198. https://doi.org/10.1007/s10518-018-0507-5
18. D'Altri AM, Messali F, Rots J, Castellazzi G, de Miranda S (2019) A damaging block-based model for the analysis of the cyclic behaviour of full-scale masonry structures. Eng Fract Mech 209:423–448. https://doi.org/10.1016/j.engfracmech.2018.11.046
19. Weyler R, Oliver J, Sain T, Cante JC (2012) On the contact domain method: a comparison of penalty and Lagrange multiplier implementations. Comput Methods Appl Mech Eng 205–208:68–82. https://doi.org/10.1016/j.cma.2011.01.011
20. Hibbitt D, Karlsson B, Sorensen P (2011) Abaqus/CAE User's Manual. Dassault Systèmes SE, USA
21. Macorini L, Izzuddin BA (2011) A non-linear interface element for 3D mesoscale analysis of brick-masonry structures. Int J Numer Meth Eng 85(12):1584–1608. https://doi.org/10.1002/nme.3046
22. Aref AJ, Dolatshahi KM (2013) A three-dimensional cyclic meso-scale numerical procedure for simulation of unreinforced masonry structures. Comput Struct 120:9–23. https://doi.org/10.1016/j.compstruc.2013.01.012
23. Abdulla KF, Cunningham LS, Gillie M (2017) Simulating masonry wall behaviour using a simplified micro-model approach. Eng Struct 151:349–365. https://doi.org/10.1016/j.engstruct.2017.08.021
24. Alforno M, Monaco A, Venuti F, Calderini C (2021) Validation of simplified micro-models for the static analysis of masonry arches and vaults. Int J Archit Herit 15(8):1196–1212. https://doi.org/10.1080/15583058.2020.1808911
25. Lourenço PB, Rots JG (1997) Multisurface interface model for analysis of masonry structures. J Eng Mech 123(7):660–668. https://doi.org/10.1061/(ASCE)0733-9399(1997)123:7(660)
26. Nie Y, Sheikh A, Visintin P, Griffith M (2023) A robust computational strategy for failure prediction of masonry structures using an improved multi-surface damage-plastic based interface model. Int J Numer Meth Eng 124(11):2498–2528. https://doi.org/10.1002/nme.7218
27. Li Y, Zeng B (2022) Modeling of masonry structures using a new 3D cohesive interface material model considering dilatancy softening. Eng Struct 2023(277):115466. https://doi.org/10.1016/j.engstruct.2022.115466
28. Khattak N, Derakhshan H, Thambiratnam DP, Malomo D, Perera NJ (2023) Modelling the in-plane/out-of-plane interaction of brick and stone masonry structures using applied element method. J Build Eng 76:107175. https://doi.org/10.1016/j.jobe.2023.107175
29. D'Altri AM, de Miranda S, Castellazzi G, Sarhosis V (2018) A 3D detailed micro-model for the in-plane and out-of-plane numerical analysis of masonry panels. Comput Struct 206:18–30. https://doi.org/10.1016/j.compstruc.2018.06.007
30. Lubliner J, Oliver J, Oller S, Oñate E (1989) A plastic-damage model for concrete. Int J Solids Struct 25(3):299–326. https://doi.org/10.1016/0020-7683(89)90050-4
31. Lee J, Fenves GL (1998) Plastic-damage model for cyclic loading of concrete structures. J Eng Mech 124(8):892–900. https://doi.org/10.1061/(ASCE)0733-9399(1998)124:8(892)
32. D'Altri AM, Sarhosis V, Milani G, Rots J, Cattari S, Lagomarsino S et al (2020) Modeling strategies for the computational analysis of unreinforced masonry structures: review and classification. Arch Comput Methods Eng 27(4):1153–1185. https://doi.org/10.1007/s11831-019-09351-x
33. Ghezelbash A, Messali F, Rots JG (2023) Finite element micro-modelling of masonry structures In: Calibration and analysis challenges. engineering mechanics institute (EMI) international conference, Palermo, Italy
34. Jafari S, Esposito R (2016) Material tests for the characterisation of replicated calcium silicate brick masonry. Delft University of Technology. Delft, Netherlands
35. Hilber HM, Hughes TJR, Talor RL (1977) Improved numerical dissipation for time integration algorithms in structural dynamics. Earthq Eng Struct Dyn 5:282–292
36. Brüls O, Golinval JC (2008) On the numerical damping of time integrators for coupled mechatronic systems. Comput Methods Appl Mech Eng 197(6–8):577–588. https://doi.org/10.1016/j.cma.2007.08.007
37. Hassan WM (2019) Numerical error assessment in nonlinear dynamic analysis of structures. HBRC J 15(1):1–31. https://doi.org/10.1080/16874048.2019.1619257
38. Vlachakis G, Giouvanidis AI, Mehrotra A, Lourenço PB (2021) Numerical block-based simulation of rocking structures using a novel universal viscous damping model. J Eng Mech. https://doi.org/10.1061/(ASCE)EM.1943-7889.0001985
39. Peña F, Lourenço PB, Campos-Costa A (2008) Experimental dynamic behavior of free-standing multi-block structures under seismic loadings. J Earthq Eng 12(6):953–979. https://doi.org/10.1080/13632460801890513
40. Housner GW (1963) The behavior of inverted pendulum structures during earthquakes. Bull Seismol Soc Am 53(2):403–417. https://doi.org/10.1785/BSSA0530020403
41. Itasca (2020) *3DEC—Three-dimensional distinct element code, Version 7.0*. Minneapolis, MN, USA: Itasca Consulting Group, Inc
42. Cruz C, Miranda E (2017) Evaluation of the Rayleigh damping model for buildings. Eng Struct 138:324–336. https://doi.org/10.1016/j.engstruct.2017.02.001
43. Psycharis IN, Drougas AE, Dasiou ME (2011) Seismic behaviour of the walls of the parthenon a numerical study. In: Papadrakakis M, Fragiadakis M, Lagaros N (eds) Computational methods in earthquake engineering. Springer, Dordrecht. https://doi.org/10.1007/978-94-007-0053-6_12

44. Galvez F, Ip K, Vaculik J, Griffith MC, Sorrentino L, Dizhur D, et al (2017) Discrete element modelling to predict failure strength of unreinforced masonry. Australian Earthquake Engineering Society 2017 Conference, Canberra, Australia
45. Galvez F, Sorrentino L, Dizhur D, Ingham JM (2022) Damping considerations for rocking block dynamics using the discrete element method. Earthq Eng Struct Dynam 51(4):935–957. https://doi.org/10.1002/eqe.3598
46. Brzev S, Anderson D (2018) seismic design guide for masonry buildings, 2nd edn. Canadian Concrete Masonry Producers Association Vancouver
47. Graziotti F, Tomassetti U, Rossi A, Kallioras S, Mandirola M, Cenja E, et al (2015) Experimental campaign on cavity walls systems representative of the Groningen building stock (Report EUC318/2015U). Pavia, Italy
48. Milani G, Valente M, Alessandri C (2018) The narthex of the church of the nativity in Bethlehem: a non-linear finite element approach to predict the structural damage. Comput Struct 207:3–18. https://doi.org/10.1016/j.compstruc.2017.03.010
49. Scacco J, Ghiassi B, Milani G, Lourenço PB (2020) A fast modeling approach for numerical analysis of unreinforced and FRCM reinforced masonry walls under out-of-plane loading. Compos B Eng 180:107553. https://doi.org/10.1016/j.compositesb.2019.107553
50. Mirmiran A, Shahawy M (1997) Dilation characteristics of confined concrete. Mech Cohes-Frict Mater 2(3):237–249. https://doi.org/10.1002/(SICI)1099-1484(199707)2:3%3c237::AID-CFM32%3e3.0.CO;2-2
51. Castellazzi G, D'Altri AM, de Miranda S, Ubertini F (2017) An innovative numerical modeling strategy for the structural analysis of historical monumental buildings. Eng Struct 132:229–248. https://doi.org/10.1016/j.engstruct.2016.11.032
52. Miglietta M, Damiani N, Guerrini G, Graziotti F (2021) Full-scale shake-table tests on two unreinforced masonry cavity-wall buildings: effect of an innovative timber retrofit. Bull Earthq Eng 19(6):2561–2596. https://doi.org/10.1007/s10518-021-01057-5
53. Tomić I, Penna A, DeJong M, Butenweg C, Correia AA, Candeias PX et al (2023) Shake table testing of a half-scale stone masonry building aggregate. Bull Earthq Eng. https://doi.org/10.1007/s10518-023-01810-y
54. Boore DM, Bommer JJ (2005) Processing of strong-motion accelerograms: needs, options and consequences. Soil Dyn Earthq Eng 25(2):93–115. https://doi.org/10.1016/j.soildyn.2004.10.007
55. Sorrentino L, Kunnath S, Monti G, Scalora G (2008) Seismically induced one-sided rocking response of unreinforced masonry façades. Eng Struct 30(8):2140–2153. https://doi.org/10.1016/j.engstruct.2007.02.021
56. Penner O, Elwood KJ (2016) Out-of-plane dynamic stability of unreinforced masonry walls in one-way bending: shake table testing. Earthq Spectra 32(3):1675–1697. https://doi.org/10.1193/011415EQS009M
57. Menon A, Magenes G (2011) Definition of seismic input for out-of-plane response of masonry walls: II formulation. J Earthq Eng 15(2):195–213. https://doi.org/10.1080/13632460903494446
58. Derakhshan H, Griffith MC, Ingham JM (2016) Out-of-plane seismic response of vertically spanning URM walls connected to flexible diaphragms. Earthq Eng Struct Dynam 45(4):563–580. https://doi.org/10.1002/eqe.2671
59. Landi L, Gabellieri R, Diotallevi PP (2015) A model for the out-of-plane dynamic analysis of unreinforced masonry walls in buildings with flexible diaphragms. Soil Dyn Earthq Eng 79:211–222. https://doi.org/10.1016/j.soildyn.2015.09.013
60. Godio M, Beyer K (2019) Quantifying the out-of-plane response of unreinforced masonry walls subjected to relative support motion. Frattura Ed Integrità Strutt 13(50):194–208. https://doi.org/10.3221/IGF-ESIS.50.17
61. Sorrentino L, Masiani R, Griffith MC (2008) The vertical spanning strip wall as a coupled rocking rigid body assembly. Struct Eng Mech 29(4):433–453. https://doi.org/10.12989/sem.2008.29.4.433
62. DeJong MJ, Dimitrakopoulos EG (2014) Dynamically equivalent rocking structures. Earthq Eng Struct Dynam 43(10):1543–1563. https://doi.org/10.1002/eqe.2410
63. Tomassetti U, Graziotti F, Penna A, Magenes G (2018) Modelling one-way out-of-plane response of single-leaf and cavity walls. Eng Struct 167:241–255. https://doi.org/10.1016/j.engstruct.2018.04.007
64. Graziotti F, Tomassetti U, Kallioras S, Penna A, Magenes G (2017) Shaking table test on a full scale URM cavity wall building. Bull Earthq Eng 15(12):5329–5364. https://doi.org/10.1007/s10518-017-0185-8
65. Kallioras S, Grottoli L, Tomassetti U, Miglietta M, Damiani N, Guerrini G, et al (2019) Experimental seismic performance assessment of Dutch unreinforced masonry buildings: identification of damage limit states (EUC183/2019U). Pavia, Italy.
66. Hallquist JO, Goudreau GL, Benson DJ (1985) Sliding interfaces with contact-impact in large-scale Lagrangian computations. Comput Methods Appl Mech Eng 51(1–3):107–137. https://doi.org/10.1016/0045-7825(85)90030-1
67. Liu GR, Quek SS (2014) FEM for 3D solid elements. The finite element method, 2nd edn. Oxford, Butterworth-Heinemann, pp 249–287. https://doi.org/10.1016/B978-0-08-098356-1.00009-6
68. Nie Y, Sheikh A, Griffith M, Visintin P (2022) A damage-plasticity based interface model for simulating in-plane / out-of-plane response of masonry structural panels. Comput Struct 260:106721. https://doi.org/10.1016/j.compstruc.2021.106721
69. Zhai C, Kong JC, Wang XH (2012) A finite element model for simulating out-of-plane behavior of masonry infilled RC frames. Appl Mech Mater 166–169:849–852. https://doi.org/10.4028/www.scientific.net/AMM.166-169.849
70. Nasiri E, Liu Y (2017) Development of a detailed 3D FE model for analysis of the in-plane behaviour of masonry infilled concrete frames. Eng Struct 143:603–616. https://doi.org/10.1016/j.engstruct.2017.04.049
71. Zeng B, Li Y, Noguez CC (2021) Modeling and parameter importance investigation for simulating in-plane and out-of-plane behaviors of un-reinforced masonry walls.

Eng Struct 248(August):113233. https://doi.org/10.1016/j.engstruct.2021.113233
72. Hibbitt HD, Karlsson BI (1979) Analysis of pipe whip. [PWR; BWR]. U.S. Department of Energy: https://doi.org/10.2172/5713659.